Superpixel-Based Weighted Sparse Regression and Spectral Similarity Constrained for Hyperspectral Unmixing

Yao Liang ⬢, Hengyi Zheng ⬢, Guoguo Yang ⬢, Qian Du ⬢, *Fellow, IEEE*, and Hongjun Su ⬢, *Senior Member, IEEE*

Abstract—**With the support of spectral libraries, sparse unmixing techniques have gradually developed. However, some existing sparse unmixing algorithms suffer from problems, such as insufficient utilization of spatial information and sensitivity to noise. To solve these problems, this article proposes a novel hyperspectral unmixing algorithm, called superpixel-based weighted sparse regression and spectral similarity constrained unmixing. In the proposed method, a precalculated weight is introduced to help enhance sparsity of abundances, which is obtained from coarse abundance estimation. It also maintains spatial consistency in a local region of a hyperspectral image to mitigate the negative influence of noise. Additionally, the method selects optimal neighborhood pixels in the local region by combining spatial and spectral information and constructs a similarity matrix to explore spectral similarity in the subspace. Meanwhile, superpixel segmentation is considered as an auxiliary method to obtain local regions in the unmixing process. Experiments performed on synthetic and real data demonstrate that the proposed method achieves more accurate abundance estimation than other comparison algorithms.**

Index Terms—**Hyperspectral unmixing (HU), spectral similarity, superpixel segmentation, weighted sparse regression.**

I. INTRODUCTION

HYPERSPECTRAL imagery (HSI) covers hundreds of contiguous narrow bands [1], enabling it to capture detailed spectral information and rich ground surface features for object identification [2], [3]. With these characteristics, hyperspectral remote sensing technology is prevalent in a great deal of works, including planetary exploration [4], environmental monitoring [5], [6], and target detection [7], [8], [9]. However, the

Yao Liang, Hengyi Zheng, and Hongjun Su are with the School of Earth Sciences and Engineering and the Jiangsu Province Engineering Research Center of Water Resources and Environment Assessment Using Remote Sensing, Hohai University, Nanjing 211100, China (e-mail: liangyao0618@163.com; z_hy2022@163.com; hjsu@hhu.edu.cn).

Guoguo Yang is with the School of Geographic Information and Tourism, Chuzhou University, Chuzhou 239000, China (e-mail: yangguoguo@chzu.edu.cn).

Qian Du is with the Department of Electrical and Computer Engineering, Mississippi State University, Starkville, MS 39762 USA (e-mail: du@ece.msstate.edu).

contradiction between its limited spatial resolution and the complexity of material distribution on the ground is the fundamental reason that mixed pixels are generally present in hyperspectral remote sensing images [10]. Unlike pure pixels, mixed pixels contain a great quantity of materials. The existence of mixed pixels poses challenges for many applications of HSI. Therefore, hyperspectral unmixing (HU) is an important research field in the process of spectral data analysis. HU refers to the process of separating mixed spectra into pure spectra (endmembers) and proportion (abundance fractions). The acquisition of endmembers and the calculation of abundances are referred to as endmember extraction and abundance estimation, respectively [11]. The design of unmixing algorithms is closely related to the spectral mixing model. According to the different forms of interaction between solar incident radiation and objects, the existing spectral mixture models are linear spectral mixture model (LSMM) and nonlinear spectral mixture model (NLSMM) [12]. LSMM considers that an observed mixed spectrum is approximately expressed as a linear combination of endmember spectra and their abundance fractions [13]. Compared to NLSMM, LSMM has computational tractability and flexibility [14]. Hence, this article focuses on LSMM-based spectral unmixing algorithms.

For LSMM, the traditional unmixing approaches involve the content related to geometry [15], [16], [17], statistics [18], and matrix decomposition [19], [20], [21], [22], [23], [24], [25], [26]. The assumption of the existence of pure endmembers needs to be satisfied in the geometry-based unmixing method, but this is not always true. NMF-based methods may produce meaningless virtual endmembers. Therefore, the accuracy of the solution is seriously limited by inaccurate endmembers in the aforementioned methods.

To solve these issues, a new framework is introduced in the field of unmixing, called sparse unmixing. It makes a major contribution to reducing the error caused by endmember extraction, considers a part of the spectra in the spectral library as endmembers, and directly estimate the abundance maps by solving constrained sparse regression problem [11]. Over the past ten years, several sparse unmixing algorithms [13], [14], [27], [28], [29], [30], [31], [32], [33] have been developed. This problem is described as a linear fitting problem, that is, an observed hyperspectral vector can be linearly fitted by spectral signatures in an available spectral library [27]. SUnSAL [13] algorithm is the starting point to use the spectral library to carry

out unmixing. The function of l_1 norm in this algorithm is to express the sparse prior of abundance vector, and the alternating direction method of multipliers (ADMM) [27] is generally regarded as the main way to solve convex optimization problems with separability. However, the SUnSAL algorithm primarily focuses on analyzing the sparsity of abundance and pays less attention on spatial structure in the image. In order to improve the unmixing accuracy, many SUnSAL-based algorithms have been created.

Sparsity is one of the important characteristics of the abundance matrix, which is usually described by l_1 norm. To obtain more accurate estimated abundance, the sparse prior of abundance is one aspect of improvement. The l_q $(0 < q < 1)$ norm strengthens the sparsity of abundance in the procedure of unmixing [34]. However, considering the fact that pixels may be mixed from the same set of endmember spectra, CLSUnSAL [35] algorithm is proposed, and the $l_{2,1}$ norm is applied through the collaborative way to express sparsity. In addition, the weight is becoming a key instrument for enhancing the ability of l_1 norm to represent sparsity [36], such as DRSU [30] algorithm. This weight consists of two parts: the first one enhances the sparsity of nonzero rows of the abundance matrix, and the second one enhances the sparsity of the nonzero entries in the nonzero rows. In short, the correct expression of the sparse prior of the abundance vector plays a positive role in HU.

On the other hand, existing research works have recognized the key role of spatial information [37], [38], [39]. Therefore, new algorithms based on spatial prior information have been proposed by many researchers. The following algorithms show that total variation (TV) is effective for the realization of abundance smoothing between adjacent pixels, including SUnSAL-TV [23] algorithm and DRSU-TV [40] algorithm. Unlike the former, the latter simultaneously explores the weighted sparsity and the spatial neighborhood information of fractional abundances. TV can only describe the relationship between a center pixel and its four neighboring pixels, but graph Laplacian is more flexible, allowing one pixel to be connected to as many similar pixels as possible [41], thus the approaches based on graph Laplacian are exploited in many works. To overcome the shortcomings of traditional hypergraphs, spectral angular distance is used as a measure to select the nearest neighbors when constructing hyperedges. This is the main innovation of AHGNTF [4] algorithm. Besides TV and graph Laplacian, low-rank representation (LRR) is popular in HU because it reveals that the abundance of similar pixels is correlated [32], [33], [42], [43], [44]. All pixels belonging to the same window are correlated, meaning they are composed of the same materials, although maybe in different proportions. This phenomenon shows that the abundance matrix has linearly correlation columns, so it has the characteristics of low rank. SUSRLR-TV [32] algorithm combines TV regularizer with low-rank attribute to realize the abundance correlation and the goal of smoothing. From the results, the algorithm reduces the range of solutions and obtain more correct abundance. Inspired by this algorithm, an algorithm considering spectral similarity and spatial low-rank attribute of local area is proposed,

which is called SBWCRLRU [33]. LSSP-RSU [45] algorithm considers spectral similarity in spatial neighborhood, and proposes a new spatial regularization.

In recent years, sparse unmixing is not limited to one sparse regression, and double regression model [14], [31], [46], [47], [48] has become popular. The double regression model achieves unmixing through two sparse regressions. The spatial contextual information obtained by solving the first sparse regression issue is used as auxiliary information to participate in the second unmixing. RDSRSU and DSGLSU algorithms both performed the first sparse regression using coarse images obtained through superpixel segmentation. The superpixel segmentation method here specifically refers to simple linear iterative clustering (SLIC) [49]. The coarse abundance contains the spatial information of the image. In the second unmixing process of DSGLSU algorithm, Laplacian regularization is used to express spectral similarity. Different from DSGLSU, RDSRSU algorithm introduces TV regularization to further improve the uniformity and smoothness of adjacent pixels in the image. The experimental results confirm that the double regression model can still produce good abundance estimation results when the image data are highly degraded.

To summarize, previous works have confirmed that unmixing approaches based on large spectral dictionaries circumvent the limitations of endmember extraction algorithms. Moreover, effectively combining spatial and spectral information can participate abundance estimation more accurately. However, how to keep the essential structure distribution of hyperspectral images and establish the unmixing model with spectral and spatial information is still an unsolved problem.

In this work, superpixel-based weighted sparse regression and spectral similarity constrained unmixing (WSRSSU) is proposed. This method considers the local spatial homogeneity of the image, and the spectral similarity between a pixel and its neighbors. The key contributions of the proposed WSRSSU algorithm can be summarized as follows.

1) In the WSRSSU, a precalculate weight obtained from coarse hyperspectral image is applied to explore the sparse feature of the abundance matrix and maintain the original spatial information of HSI. Then, the influence of noise is reduced by using the local spatial homogeneity of the image.

2) In the WSRSSU, considering the limitation of using only distance to select neighboring pixels, a new criterion is applied to consider both spatial structure information and spectral information to select the optimal neighboring pixels. Then, the similarity weight is constructed to explore the spectral similarity in the subspace.

The rest of this article is arranged as follows. Section II presents the related work, including LMM and sparse unmixing. Section III introduces the details of the proposed WSRSSU algorithm. Section IV focuses on the performance evaluation on synthetic and real data. Section V discusses the influence of parameters on algorithm performance. Finally, Section VI concludes this article.

II. RELATED WORK

A. Linear Mixture Model

The LMM model assumes that each photon can only interact with one object, and the signal of the object is superimposed into the pixel spectrum. The LMM model can be described as

$$\boldsymbol{Y} = \boldsymbol{A}\boldsymbol{X} + \boldsymbol{E} \tag{1}$$

where $\boldsymbol{Y} = [\boldsymbol{y}_1, \cdots, \boldsymbol{y}_N] \in R^{L \times N}$ is the image matrix rearranged for an HSI cube, including N L-dimensional pixel vectors. $\boldsymbol{A} \in R^{L \times M}$ is a rich collection of spectral signatures of ground objects, which may be from a spectral library, and M is the number of materials contained in the image. $\boldsymbol{X} = [\boldsymbol{x}_1, \cdots, \boldsymbol{x}_N] \in R^{M \times N}$ is the abundance matrix, and $\boldsymbol{E} \in R^{L \times N}$ represents random noise of data. The physical meaning of $\boldsymbol{X}_{i,j}$ is the area proportion of the jth endmember in the ith pixel. Theoretically, the abundance matrix should obey two indispensable constraints: abundance nonnegativity constraint (ANC) and abundance sum-to-one constraint (ASC), which can be expressed as

$$ANC\colon \boldsymbol{X} \geq 0$$
$$ASC\colon 1^T \boldsymbol{X} = 1^T \tag{2}$$

where $\mathbf{1}$ represents a column vector with all elements being 1.

In practice, the ASC is rarely satisfied [11]. Thus, in this article, only the ANC is imposed on (1), resulting in the following formula for unmixing:

$$\arg \min_{\boldsymbol{X}} \frac{1}{2} \|\boldsymbol{Y} - \boldsymbol{A}\boldsymbol{X}\|_F^2 + l_{R^+}(\boldsymbol{X}). \tag{3}$$

B. Sparse Unmixing

The spectral library participating in unmixing consists of a great quantity of spectral signatures, but only a few of them are involved in the unmixing model, resulting in many zero elements in the fractional abundances. Therefore, the abundance matrix is inherently sparse, and the objective function can be described as follows:

$$\arg \min_{\boldsymbol{X}} \frac{1}{2} \|\boldsymbol{Y} - \boldsymbol{A}\boldsymbol{X}\|_F^2 + \lambda \|\boldsymbol{X}\|_0 + l_{R^+}(\boldsymbol{X}) \tag{4}$$

where $\|\cdot\|_F$ is the Frobenius norm, $\|\boldsymbol{Y} - \boldsymbol{A}\boldsymbol{X}\|_F^2$ is the fidelity item representing the difference between the reconstruct signal and the original signal, $\|\boldsymbol{X}\|_0$ represents the number of nonzero elements of $\boldsymbol{X}$, and λ is a positive parameter controlling the relative weight of the fidelity item and the regularization term. Here, $l_{R^+}(\boldsymbol{X})$ is an indicator function used to control the estimated abundance matrix $\boldsymbol{X}$ to be nonnegative, shown as
$l_{R^+}(\boldsymbol{X}) = \begin{cases} 0 & \boldsymbol{X} \geq 0 \\ +\infty & \boldsymbol{X} < 0 \end{cases}$.

The optimization problem (4) is NP hard [50]. To solve this kind of problem, replace the l_0 norm with the l_1 norm [27] to achieve the purpose of convex relaxation. Then, the convex optimization problem is converted into

$$\arg \min_{\boldsymbol{X}} \frac{1}{2} \|\boldsymbol{Y} - \boldsymbol{A}\boldsymbol{X}\|_F^2 + \lambda \|\boldsymbol{X}\|_{1,1} + l_{R^+}(\boldsymbol{X}) \tag{5}$$

where $\|\boldsymbol{X}\|_{1,1} = \sum_{j=1}^{N} \|\boldsymbol{x}_j\|_1$, $\boldsymbol{x}_j$ is the abundance vector of an L-dimensional pixel. The optimization problem in (5) can be effectively solved through an ADMM algorithm.

III. SPARSE UNMIXING VIA WSRSSU

The algorithm focuses on local spectral similarity and local spatial homogeneity. How to construct local regions is an issue that needs to be solved. Research shows that a superpixel segmentation method can obtain homogeneous regions to assist hyperspectral data analysis [51]. SLIC creates irregular pixel blocks with visual significance simply and efficiently. So, the WSRSSU model is proposed based on SLIC. Its schematic is summarized as in Fig. 1.

A. Superpixel Segmentation

The purpose of superpixel segmentation is to divide an image into multiple highly similar regions, each of which is called a superpixel [52]. In this article, SLIC is adopted for hyperspectral image segmentation. This algorithm needs a parameter: S, where S represents the number of superpixels. SLIC first generates an initial set of superpixels, each of which is a regular grid region containing N/S pixels. The center of each grid is the initialized seed point (cluster center). In hyperspectral images, distance measurement is constructed based on the spectra and position of pixels. The similarity between each pixel and the seed point is obtained based on distance measurement. Each pixel is assigned to the nearest seed point to ensure that pixels with similar characteristics are grouped together. This algorithm iteratively updates the clustering center based on the average of the spectral and spatial information of all pixels in each cluster. This process continues until the cluster center not change significantly. The final segmentation result is shown in Fig. 2

$$d_{\text{spectral}}(i, j) = \|\boldsymbol{y}_i - \boldsymbol{y}_j\|_2^2 \tag{6}$$

$$d_{\text{spatial}}(i, j) = \sqrt{(p_i - p_j)^2 + (q_i - q_j)^2} \tag{7}$$

$$D' = \sqrt{d_{\text{spectral}}^2 + \alpha d_{\text{spatial}}^2} \tag{8}$$

where $\boldsymbol{y}_i$ and $\boldsymbol{y}_j$ represent spectral of pixel i and j, (p_i, q_i) and (p_j, q_j) represent position of pixel i and j. d_{spectral} and d_{spatial} represent spectral and spatial distances, respectively.

B. Weighted Sparse Regression

Noise plays an obstacle role in the processing of hyperspectral images. An HSI is always interfered with by noise, which affects the unmixing accuracy. To solve this problem, the image is reconstructed using local spatial homogeneity, and the spatial weight matrix $\boldsymbol{W}_{\text{spa}}$ is constructed using the reconstructed image for unmixing.

1) Step 1: Coarse-Scale Image Approximation: First, the primitive HSI $\boldsymbol{Y} \in R^{L \times N}$ is segmented into S superpixels by the SLIC algorithm. Let $\boldsymbol{Y}_t \in R^{L \times N_t}$ ($t = 1, \ldots, S$, $\sum_{t=1}^{S} N_t = N$) be the component of Y corresponding to the tth superpixel and $\boldsymbol{y}_i \in R^{L \times 1}$ ($i = 1 \cdots N_t$) be a column vector in $\boldsymbol{Y}_t$. Then, the spectral average value of
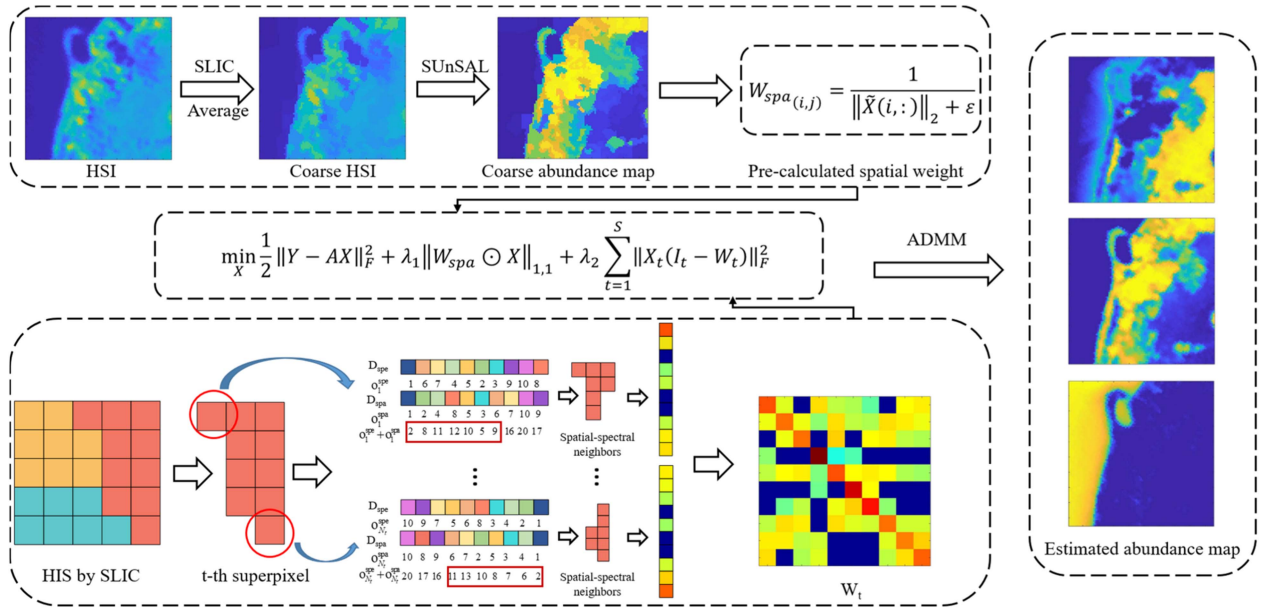
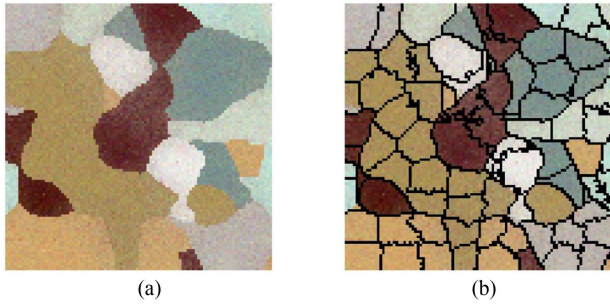Fig. 1.   Schematic of the WSRSSU approach.

Fig. 2.   SLIC for hyperspectral image. (a) Original image. (b) Segmentation image.

all pixels in each superpixel block replaces the original spectral value of all pixels in the block.

A coarse-scale image $\tilde{Y} \in R^{L \times N}$ is reconstructed as

$$\tilde{y}_t = \frac{1}{N_t} \sum_{i=1}^{N_t} y_i \qquad (9)$$

where $\tilde{y}_t$ represents the spectral mean value in the tth superpixel block. The spectral values of all pixels in the tth superpixel block are assigned as $\tilde{y}_t$. The coarse superpixel $\tilde{Y}_t$ is obtained accordingly. The coarse-scale image $\tilde{Y}$ is obtained by arranging each superpixel block $\tilde{Y}_t$ according to pixel position.

2) Step 2: Spatial Weight Matrix Construction: The coarse abundance matrix $\tilde{X}$ can be obtained by using the SUnSAL algorithm. The formula is described as follows:

$$\arg \min_{\tilde{X}} \frac{1}{2} \|\tilde{Y} - A\tilde{X}\|_F^2 + \lambda \|\tilde{X}\|_{1,1} + l_{R^+}\left(\tilde{X}\right). \qquad (10)$$

To effectively reduce the impact of noise, the spectral mean is used to represent the average spectral level of each superpixel to construct a coarse-scale image with local spatial uniformity. Therefore, coarse abundance matrix $\tilde{X}$ and weight matrix $\boldsymbol{W}_{\text{spa}}$ are less sensitive to noise.

The weight matrix $\boldsymbol{W}_{\text{spa}}$ can be calculated as

$$\boldsymbol{W}_{\text{spa}(i,j)} = \frac{1}{\|\tilde{\boldsymbol{X}}\,(i,:)\|_2 + \varepsilon}, i = 1 \cdots M, j = 1 \cdots N \quad (11)$$

where $\boldsymbol{W}_{\text{spa}(i,j)}$ is the element in the ith row and jth column of $\boldsymbol{W}_{\text{spa}}$. $\boldsymbol{W}_{\text{spa}}$ is used to minimize the weighted l_1 norm to enhance sparsity of $\boldsymbol{X}$ and keeps the spatial information inside each superpixel. It is applied to unmixing, shown as

$$\min_{\boldsymbol{X}} \|\boldsymbol{W}_{\text{spa}} \odot \boldsymbol{X}\|_{1,1} \qquad (12)$$

where $\odot$ is Khatri–Rao product, which is used to multiply the elements at corresponding positions of two matrices.

C. Spectral Similarity Constrained

Pixels in a local area often have similar characteristics and spectral values [20]. Each pixel can be approximated by the linear representation of all pixels in the same subspace in which it resides [53]. Therefore, in this article, we approximate each pixel using its similar neighbors.

1) Step 1: Determination of Optimal Neighbors: The existence of spatial correlation between pixels in local areas means that the spatial distribution of pixels and features is consistent within a certain range. Therefore, taking action from joint spatial and spectral information can determine more suitable neighbors [54]. Euclidean distances are used as the basic method to calculate the spectral and spatial distances between pixels. Taking the tth superpixel as an example, the spectral distance is obtained

by calculating the l_2 norm of two spectral vectors as

$$d_{\mathrm{spe}}\left(\boldsymbol{y}_t^i, \boldsymbol{y}_t^j\right) = \|\boldsymbol{y}_t^i - \boldsymbol{y}_t^j\|_2, i, j = 1 \cdots N_t \qquad (13)$$

where N_t represents the number of pixels contained in the tth superpixel, $\boldsymbol{y}_t^i$ represents the spectral value of the ith pixel in the tth superpixel, and $\boldsymbol{y}_t^j$ and $\boldsymbol{y}_t^i$ have similar meanings. The spectral ordinal number $O_i^{\mathrm{spe}} = [o_1^{\mathrm{spe}}, o_2^{\mathrm{spe}}, \cdots o_{N_t}^{\mathrm{spe}}]$ is defined in such a way that spectral distances are sorted from small to large, meaning that the farther the distance, the greater the ordinal number. The ordinal number is from 1 to N_t.

Let the coordinates of $\boldsymbol{y}_t^i$ and $\boldsymbol{y}_t^j$ in the HSI be denoted as (p_i, q_i) and (p_j, q_j), respectively. Then, the spatial distances are calculated by coordinates as

$$d_{\mathrm{spa}}\left(\boldsymbol{y}_t^i, \boldsymbol{y}_t^j\right) = \sqrt{(p_i - p_j)^2 + (q_i - q_j)^2}, i, j = 1 \cdots N_t. \qquad (14)$$

The spatial ordinal number $O_i^{\mathrm{spa}} = [o_1^{\mathrm{spa}}, o_2^{\mathrm{spa}}, \cdots o_{N_t}^{\mathrm{spa}}]$ is defined to be similar to O_i^{spe}. Then, the two ordinal numbers O_i^{spe} and O_i^{spa} can be summed to obtain a new ordinal number $O_i^{\mathrm{spe+spa}} = [o_1^{\mathrm{spe}} + o_1^{\mathrm{spa}}, o_2^{\mathrm{spe}} + o_2^{\mathrm{spa}}, \cdots o_{N_t}^{\mathrm{spe}} + o_{N_t}^{\mathrm{spa}}]$. The final ordinal number reflects the spatial–spectral information between pixels. Using an ordinal sequence ranging from small to large, K pixels are selected as the spatial–spectral neighbors of the ith pixel.

2) Step 2: Similarity Matrix Construction: Considering that the pixels in the local region have similar spectral characteristics, a similarity matrix is constructed to approximate the original hyperspectral data. In order to reduce the time cost, SLIC is used to divide the image into several superpixels and establish a similarity matrix for each superpixel. The original data are approximated by the optimal neighbors and the similarity matrix to achieve the purpose of similarity constraint.

Taking the tth superpixel as an example, the formula is described as follows:

$$\boldsymbol{Y}_t = \boldsymbol{Y}_t \boldsymbol{W}_t \qquad (15)$$

where $\boldsymbol{Y}_t$ is the tth superpixel, and $\boldsymbol{W}_t \in R^{N_t \times N_t}$ is the similarity matrix corresponding to the tth superpixel. It is a sparse matrix, in which the elements at the location of the optimal neighbors are nonzero values, and the elements at other locations are zero values. Its (i, j)th element can be computed as

$$\boldsymbol{W}_{t_{(i,j)}} = \frac{1}{H} \exp^{-\frac{\|\boldsymbol{y}_i - \boldsymbol{y}_j\|^2}{\sigma}}, i = 1 \cdots N_t, \mathrm{j} \in G_t. \qquad (16)$$

Here, G_t refers to the index of the optimal neighbors' pixel in the superpixel block. $\boldsymbol{W}_{t_{(i,j)}}$ describes the similarity between the pixel $\boldsymbol{y}_i$ and the pixel $\boldsymbol{y}_j$ in the neighbor region, and $\sum_j \boldsymbol{W}_{t_{(i,j)}} = 1$. H is a regularization term defined as

$$H = \sum_{\mathrm{j} \in G_t} \exp^{-\frac{\|\boldsymbol{y}_i - \boldsymbol{y}_j\|^2}{\sigma}} \qquad (17)$$

where σ is a smoothing kernel [55]. In an image, the similarity of pixels inevitably has similar abundance relationships [45]. Based on formula (15), the similarity constraint of abundance

can be expressed as follows:

$$\min_{\boldsymbol{X}_t} \|\boldsymbol{X}_t \left(\boldsymbol{I}_t - \boldsymbol{W}_t\right)\|_F^2 \qquad (18)$$

where $\boldsymbol{I}_t \in R^{N_t \times N_t}$ is the identity matrix.

D. Formulation of Proposed WSRSSU Model

WSRSSU algorithm is described as follows:

$$\arg\min_{\boldsymbol{X}} \frac{1}{2}\|\boldsymbol{Y} - \boldsymbol{A}\boldsymbol{X}\|_F^2 + \lambda_1\|\boldsymbol{W}_{spa} \odot \boldsymbol{X}\|_{1,1}$$
$$+ \lambda_2 \sum_{t=1}^{S} \|\boldsymbol{X}_t \left(\boldsymbol{I}_t - \boldsymbol{W}_t\right)\|_F^2 + l_{R^+}\left(\boldsymbol{X}\right) \qquad (19)$$

where $\boldsymbol{W}_{\mathrm{spa}}$ and $\boldsymbol{W}_t$ were introduced in Sections III-B and III-C, respectively.

To solve this problem using ADMM, the original problem is split into several small problems by introducing auxiliary variables. The equivalent problem of (19) can be described as

$$\arg\min_{\boldsymbol{U}, \boldsymbol{V}_1, \boldsymbol{V}_2, \boldsymbol{V}_3, \boldsymbol{V}_4} \frac{1}{2}\|\boldsymbol{Y} - \boldsymbol{V}_1\|_F^2 + \lambda_1\|\boldsymbol{W}_{\mathrm{spa}} \odot \boldsymbol{V}_2\|_{1,1}$$
$$+ \lambda_2 \sum_{t=1}^{S} \|\boldsymbol{V}_{3_t} \left(\boldsymbol{I}_t - \boldsymbol{W}_t\right)\|_F^2 + l_{R^+}\left(\boldsymbol{V}_4\right)$$
$$\mathrm{s.t.}\ \boldsymbol{V}_1 = \boldsymbol{A}\boldsymbol{U}, \boldsymbol{V}_2 = \boldsymbol{U}, \boldsymbol{V}_3 = \boldsymbol{U}, \boldsymbol{V}_4 = \boldsymbol{U}. \qquad (20)$$

The first item is data fidelity term, the second term is weighted sparse term, the third term is spectral similarity constraint term, and the last term is nonnegative constraint term.

Optimization of (20) for a simplified version yields

$$\min_{\boldsymbol{U}, \boldsymbol{V}} g\left(\boldsymbol{U}, \boldsymbol{V}\right)\ \mathrm{s.t.}\ \boldsymbol{G}\boldsymbol{U} + \boldsymbol{B}\boldsymbol{V} = 0 \qquad (21)$$

where $\boldsymbol{V} = (\boldsymbol{V}_1, \boldsymbol{V}_2, \boldsymbol{V}_3, \boldsymbol{V}_4)^T$, $g(\boldsymbol{U}, \boldsymbol{V}) \equiv \min_{\boldsymbol{U}, \boldsymbol{V}_1, \boldsymbol{V}_2, \boldsymbol{V}_3, \boldsymbol{V}_4} \frac{1}{2}\|\boldsymbol{Y} - \boldsymbol{V}_1\|_F^2 + \lambda_1\|\boldsymbol{W}_{\mathrm{spa}} \odot \boldsymbol{V}_2\|_{1,1} + \lambda_2 \sum_{t=1}^{S} \|\boldsymbol{V}_{3_t}(\boldsymbol{I}_t - \boldsymbol{W}_t)\|_F^2 + l_{R^+}(\boldsymbol{V}_4)$, and

$$\boldsymbol{G} = \begin{bmatrix} \boldsymbol{A} \\ \boldsymbol{I} \\ \boldsymbol{I} \\ \boldsymbol{I} \end{bmatrix}, \mathbf{B} = \begin{bmatrix} -\boldsymbol{I} & 0 & 0 & 0 \\ 0 & -\boldsymbol{I} & 0 & 0 \\ 0 & 0 & -\boldsymbol{I} & 0 \\ 0 & 0 & 0 & -\boldsymbol{I} \end{bmatrix}.$$

The constrained problem (21) is transformed into an unconstrained problem (22) by using the augmented Lagrange algorithm

$$\mathcal{L}\left(\boldsymbol{U}, \boldsymbol{V}, \boldsymbol{D}\right) = g\left(\boldsymbol{U}, \boldsymbol{V}\right) + \frac{\mu}{2}\|\boldsymbol{G}\boldsymbol{U} + \boldsymbol{B}\boldsymbol{V} - \boldsymbol{D}\|_F^2 \qquad (22)$$

where $\mu > 0$ is a penalty parameter, and $\boldsymbol{D} = (\boldsymbol{D}_1, \boldsymbol{D}_2, \boldsymbol{D}_3, \boldsymbol{D}_4)^T$ is the Lagrange multipliers. During each iteration of $\mathcal{L}(\boldsymbol{U}, \boldsymbol{V}, \boldsymbol{D})$, $\boldsymbol{U}$, $\boldsymbol{V}$, and $\boldsymbol{D}$ are updated gradually.

When the variable is only $\boldsymbol{U}$, the optimization problem is

$$\boldsymbol{U}^{(m+1)} = \arg\min_{\boldsymbol{U}} \frac{\mu}{2}\|\boldsymbol{A}\boldsymbol{U} - \boldsymbol{V}_1^{(m)} - \boldsymbol{D}_1^{(m)}\|_F^2$$
$$+ \frac{\mu}{2}\|\boldsymbol{U} - \boldsymbol{V}_2^{(m)} - \boldsymbol{D}_2^{(m)}\|_F^2$$

$$+ \frac{\mu}{2}\|\boldsymbol{U} - \boldsymbol{V}_3^{(m)} - \boldsymbol{D}_3^{(m)}\|_F^2$$

$$+ \frac{\mu}{2}\|\boldsymbol{U} - \boldsymbol{V}_4^{(m)} - \boldsymbol{D}_4^{(m)}\|_F^2. \tag{23}$$

Taking the partial derivative of (23) results in

$$\boldsymbol{U}^{(m+1)} = \left(\boldsymbol{A}^T\boldsymbol{A} + 3\boldsymbol{I}\right)^{-1} \left(\boldsymbol{A}^T \left(\boldsymbol{V}_1^{(m)} + \boldsymbol{D}_1^{(m)}\right)\right.$$

$$+ \left(\boldsymbol{V}_2^{(m)} + \boldsymbol{D}_2^{(m)}\right)$$

$$+ \left(\boldsymbol{V}_3^{(m)} + \boldsymbol{D}_3^{(m)}\right)$$

$$\left. + \left(\boldsymbol{V}_4^{(m)} + \boldsymbol{D}_4^{(m)}\right)\right). \tag{24}$$

When the variable is only $\boldsymbol{V}_1$, the optimization problem is

$$\boldsymbol{V}_1^{(m+1)} = \arg\min_{\boldsymbol{V}_1} \frac{1}{2}\|\boldsymbol{Y} - \boldsymbol{V}_1\|_F^2$$

$$+ \frac{\mu}{2}\|\boldsymbol{A}\boldsymbol{U}^{(m+1)} - \boldsymbol{V}_1 - \boldsymbol{D}_1^{(m)}\|_F^2. \tag{25}$$

Taking the partial derivative of (25) for $\boldsymbol{V}_1$

$$\boldsymbol{V}_1^{(m+1)} = \frac{1}{1+\mu} \left[\boldsymbol{Y} + \mu\left(\boldsymbol{A}\boldsymbol{U}^{(m+1)} - \boldsymbol{D}_1^{(m)}\right)\right]. \tag{26}$$

When the variable is only $\boldsymbol{V}_2$, the optimization problem is

$$\boldsymbol{V}_2^{(m+1)} = \arg\min_{\boldsymbol{V}_2} \lambda_1\|\boldsymbol{W}_{\text{spa}} \odot \boldsymbol{V}_2\|_{1,1}$$

$$+ \frac{\mu}{2}\|\boldsymbol{U}^{(m+1)} - \boldsymbol{V}_2 - \boldsymbol{D}_2^{(m)}\|_F^2. \tag{27}$$

The partial derivative of (27) results in

$$\boldsymbol{V}_2^{(m+1)} = \text{soft}\left(\boldsymbol{U}^{(m+1)} - \boldsymbol{D}_2^{(m)}, \frac{\lambda_1}{\mu}\boldsymbol{W}_{\text{spa}}\right). \tag{28}$$

Here, $\text{soft}(\cdot, \tau)$ is the soft-threshold function applied to each element in the matrix [56], $\text{soft}(\mathcal{U}, a) \equiv \text{sign}(\mathcal{Y})\max\{|\mathcal{U}| - a, 0\}$.

When the variable is only $\boldsymbol{V}_3$, the optimization problem is

$$\boldsymbol{V}_3^{(m+1)} = \arg\min_{\boldsymbol{V}_3} \lambda_2 \sum_{t=1}^{S} \|\boldsymbol{V}_{3t}\left(\boldsymbol{I}_t - \boldsymbol{W}_t\right)\|_F^2$$

$$+ \frac{\mu}{2}\|\boldsymbol{U}^{(m+1)} - \boldsymbol{V}_3 - \boldsymbol{D}_3^{(m)}\|_F^2. \tag{29}$$

After calculating the partial derivative of (29)

$$\boldsymbol{V}_{3t}^{(m+1)} = \mu\left(\boldsymbol{U}^{(m+1)} - \boldsymbol{D}_3^{(m)}\right)_t$$

$$\left(2\lambda_2\left(\boldsymbol{I}_t - \boldsymbol{W}_t\right)\left(\boldsymbol{I}_t - \boldsymbol{W}_t\right)^T + \mu\boldsymbol{I}\right)^{-1}. \tag{30}$$

Here, $\boldsymbol{V}_{3t}$ is the component corresponding to tth superpixel block in $\boldsymbol{V}_3$. Arrange $\boldsymbol{V}_{3t}$ according to pixel position to get $\boldsymbol{V}_3$.

When the variable is only $\boldsymbol{V}_4$, the optimization problem is

$$\boldsymbol{V}_4^{(m+1)} = \arg\min_{\boldsymbol{V}_4} l_{R^+}\left(\boldsymbol{V}_4\right)$$

$$+ \frac{\mu}{2}\|\boldsymbol{U}^{(m+1)} - \boldsymbol{V}_4 - \boldsymbol{D}_4^{(m)}\|_F^2. \tag{31}$$

Calculating the partial derivative of (31) to generate the result of V_4

$$\boldsymbol{V}_4^{(m+1)} = \max\left(\boldsymbol{U}^{(m+1)} - \boldsymbol{D}_4^{(m)}, 0\right). \tag{32}$$

Finally, the Lagrange multipliers are sequentially updated as

$$\boldsymbol{D}_1^{(m+1)} = \boldsymbol{D}_1^{(m)} - \boldsymbol{A}\boldsymbol{U}^{(m+1)} + \boldsymbol{V}_1^{(m+1)} \tag{33}$$

$$\boldsymbol{D}_2^{(m+1)} = \boldsymbol{D}_2^{(m)} - \boldsymbol{U}^{(m+1)} + \boldsymbol{V}_2^{(m+1)} \tag{34}$$

$$\boldsymbol{D}_3^{(m+1)} = \boldsymbol{D}_3^{(m)} - \boldsymbol{U}^{(m+1)} + \boldsymbol{V}_3^{(m+1)} \tag{35}$$

$$\boldsymbol{D}_4^{(m+1)} = \boldsymbol{D}_4^{(m)} - \boldsymbol{U}^{(m+1)} + \boldsymbol{V}_4^{(m+1)}. \tag{36}$$

For clarity, the pseudocode of WSRSSU algorithm is summarized as Algorithm 1.

According to Algorithm 1, the computation complexity of $\boldsymbol{U}$ and $\boldsymbol{V}_3$ is relatively high, so they dominate the complexity of the entire algorithm. The terms $\left(\boldsymbol{A}^T\boldsymbol{A} + 3\boldsymbol{I}\right)^{-1}$ and $\left(2\lambda_2(\boldsymbol{I}_t - \boldsymbol{W}_t)(\boldsymbol{I}_t - \boldsymbol{W}_t)^T + \mu\boldsymbol{I}\right)^{-1}$ can be precomputed. Therefore, $\boldsymbol{U}^{(m+1)}$ complexity is $\mathcal{O}(MNL)$ and $\boldsymbol{V}_3^{(m+1)}$ complexity is $\mathcal{O}(SMN_t^2)$. The complexity of the WSRSSU algorithm is $\mathcal{O}(MNL) + \mathcal{O}(SMN_t^2)$.

IV. EXPERIMENTS

The performance of the WSRSSU algorithm is evaluated by using two synthetic datasets and three real hyperspectral images. Comparison algorithms involved in the experiment include SUnSAL [27], SUnSAL-TV [28], MUA$_{\text{SLIC}}$ [31], SUSRLR-TV [32], SBWCRLRU [33], and RDSRSU [14]. For quantitative comparison, two image quality evaluation indicators are adopted. The signal-to-reconstruction error (SRE, measured in decibel) [32] is used to evaluate the difference between the original signal and the reconstructed signal, which is defined as

$$\text{SRE} = 10\log_{10}\left(\frac{E\left[\|\boldsymbol{X}\|_2^2\right]}{E\left[\|\boldsymbol{X} - \hat{\boldsymbol{X}}\|_2^2\right]}\right) \tag{37}$$

where $\boldsymbol{X}$ and $\hat{\boldsymbol{X}}$ represent the true and the estimated abundance, respectively. Higher SRE value means more accurate abundance estimation result.

Another image quality evaluation index is root-mean-square error (RMSE) [44]. RMSE is used to describe the difference between the original abundance and the estimated abundance by the algorithm. The lower the RMSE, the more similar the original abundance and estimated abundance. The RMSE is defined as

$$\text{RMSE} = \sqrt{\frac{\|\boldsymbol{X} - \hat{\boldsymbol{X}}\|_F^2}{LN}}. \tag{38}$$

Lower RMSE value means more accurate abundance estimation result.

A. Experiments on Synthetic Data

1) Data Details: Two synthetic datasets are generated with the same spectral library $\boldsymbol{A} \in R^{224 \times 240}$. The spectral library
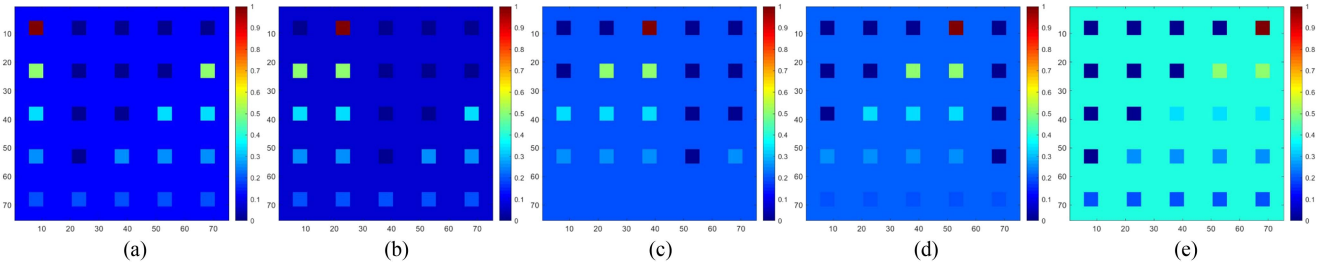
Fig. 3. Ground truth of SD1. (a)–(e) True spatial distribution of endmember 1–5, respectively.

Algorithm 1: Instructions of WSRSSU Algorithm.

Step 1:

1: Input: **Y**, **A**, the number of superpixels S

2: Use SLIC algorithm for local area acquisition

3: Calculate (9) to get the coarse image $\tilde{\boldsymbol{Y}}$

4: Calculate (10) to get the coarse abundance $\tilde{\boldsymbol{X}}$

5: Calculate (11) to get the weight $\boldsymbol{W}_{spa}$

Step 2:

1: **Initialization:** set $m = 0$, choose $\lambda_1, \lambda_2, \mu, \varepsilon > 0$
$\boldsymbol{U}^{(0)}, \boldsymbol{V}_1^{(0)}, \boldsymbol{V}_2^{(0)}, \boldsymbol{V}_3^{(0)}, \boldsymbol{V}_4^{(0)}, \boldsymbol{D}_1^{(0)}, \boldsymbol{D}_2^{(0)}, \boldsymbol{D}_3^{(0)}, \boldsymbol{D}_4^{(0)}$

2: **Repeat:**

3: $\boldsymbol{U}^{(m+1)} \leftarrow (\boldsymbol{A}^T\boldsymbol{A} + 3\boldsymbol{I})^{-1}(\boldsymbol{A}^T(\boldsymbol{V}_1^{(m)} + \boldsymbol{D}_1^{(m)})$
$+ (\boldsymbol{V}_2^{(m)} + \boldsymbol{D}_2^{(m)}) + (\boldsymbol{V}_3^{(m)} + \boldsymbol{D}_3^{(m)}) +$
$(\boldsymbol{V}_4^{(m)} + < ?hsp12pt? > \boldsymbol{D}_4^{(m)}))$

4: $\boldsymbol{V}_1^{(m+1)} \leftarrow \frac{1}{1+\mu}[\boldsymbol{Y} + \mu(\boldsymbol{A}\boldsymbol{U}^{(m+1)} - \boldsymbol{D}_1^{(m)})]$

5: $\boldsymbol{V}_2^{(m+1)} \leftarrow soft(\boldsymbol{U}^{(m+1)} - \boldsymbol{D}_2^{(m)}, \frac{\lambda_1}{\mu}\boldsymbol{W}_{spa})$

6: **for** t = 1 to S

7: Determine of optimized neighbors according to (13) and (14)

8: Calculate $\boldsymbol{W}_t$ according to (16) and (17)

9: $\boldsymbol{V}_{3_t}^{(m+1)} = \mu(\boldsymbol{U}^{(m+1)} - \boldsymbol{D}_3^{(m)})_t$
$(2\lambda_2(\boldsymbol{I}_t - \boldsymbol{W}_t)(\boldsymbol{I}_t - \boldsymbol{W}_t)^T + \mu\boldsymbol{I})^{-1}$

10: Rearrange $\boldsymbol{V}_{3_t}^{(m+1)}$ according to the index to get $\boldsymbol{V}_3^{(m+1)}$

11: **end for**

12: $\boldsymbol{V}_4^{(m+1)} \leftarrow \max(\boldsymbol{U}^{(m+1)} - \boldsymbol{D}_4^{(m)}, 0)$

13: $\boldsymbol{D}_1^{(m+1)} \leftarrow \boldsymbol{D}_1^{(m)} - \boldsymbol{A}\boldsymbol{U}^{(m+1)} + \boldsymbol{V}_1^{(m+1)}$

14: $\boldsymbol{D}_2^{(m+1)} \leftarrow \boldsymbol{D}_2^{(m)} - \boldsymbol{U}^{(m+1)} + \boldsymbol{V}_2^{(m+1)}$

15: $\boldsymbol{D}_3^{(m+1)} \leftarrow \boldsymbol{D}_3^{(m)} - \boldsymbol{U}^{(m+1)} + \boldsymbol{V}_3^{(m+1)}$

16: $\boldsymbol{D}_4^{(m+1)} \leftarrow \boldsymbol{D}_4^{(m)} - \boldsymbol{U}^{(m+1)} + \boldsymbol{V}_4^{(m+1)}$

17: **Update loops iteration:** $m \leftarrow m + 1$

18: until some stopping criterion is satisfied.

---

includes 240 materials, covering 224 bands from visible light to short-wave infrared [11]. Two synthetic data cubes were obtained by mixing endmembers with specific proportions, which are described in detail as follows.

Synthetic Data 1 (SD1): SD1 is a square data composed of 5625 pixels, with 224 bands per pixel. Its formation depends on five endmembers in the spectral library **A**. There are pure regions and mixed regions in these data. The mixed region is obtained by mixing ranging between two and five endmembers. It is worth mentioning that the background is constructed with five endmembers in the proportions of 0.1149, 0.0741, 0.2003, 0.2055, and 0.4051 [28]. The synthetic data are arranged in a square in space. Fig. 3 lists five authentic abundance maps of SD1. In order to make the synthetic data closer to the real hyperspectral data, different levels of Gaussian noise are added. Therefore, the SNR of SD1 used in the experiment is 20, 30, and 40 dB, respectively.

Synthetic Data 2 (SD2): SD2 is the same square data as SD1 and consists of 10 000 pixels and 224 bands. Nine spectral signatures are selected from the spectral library **A** as endmembers, following the abundance distribution in Fig. 4, and noise is added similarly.

2) Result Comparison: Table I shows the results of different unmixing algorithms on both SD1 and SD2, covering all three SNR levels. The table includes the values of SRE and RMSE, with the best result for each algorithm being bolded. It is clear from the table that the proposed WSRSSU algorithm outperforms other comparison algorithms, regardless of which synthetic data and SNR level are used.

First, the experimental results in Table I are compared horizontally, meaning that the changes of different algorithms are analyzed when the SNR is the same. SUnSAL, which is the most classical sparse unmixing method, has the worst results among all the algorithms compared. The other five comparison algorithms are superior to SUnSAL because they use spatial information for unmixing. Among the three algorithms that use TV regularizer for unmixing, SUnSAL-TV directly adds TV regularizer to the sparse unmixing method, whereas SUSRLR-TV introduces LRR as a spatial constraint in the optimization process. On the other hand, RDSRSU combines TV regularizer with weighted sparse representation. As can be observed from Table I, the RDSRSU algorithm outperforms the other two algorithms using the TV regularizer, indicating the advantages of weighted sparse representation in HU. In contrast, the WSRSSU algorithm utilizes both spatial and spectral information for unmixing, and uses spatial weights to enhance sparsity and reduce the impact of noise, resulting in superior performance compared to other algorithms.

Second, in a longitudinal comparison of the same algorithm across different SNRs, increasing the SNR tends to result in
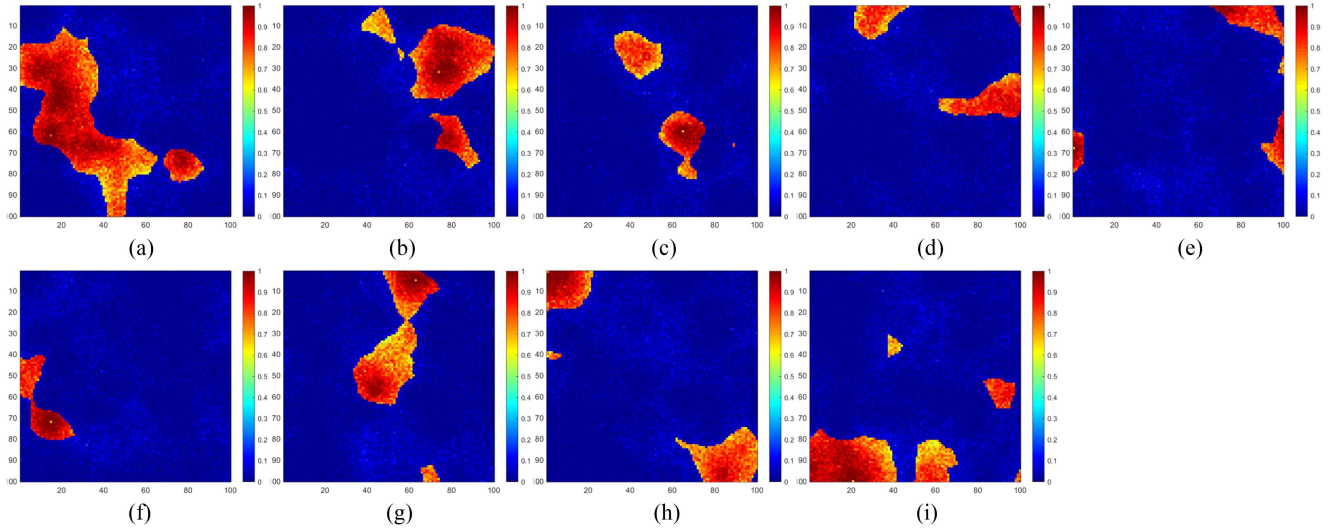
Fig. 4.   Ground truth of SD2. (a)–(i) True spatial distribution of endmember 1–9, respectively.

TABLE I
EVALUATION INDEXES VALUES OF SEVEN ALGORITHMS ON SYNTHETIC DATA

Data	SNR	Evaluation indexes	SUnSAL	SUnSAL-TV	MUA$_{SLIC}$	SUSRLR-TV	SBWCRLRU	RDSRSU	WSRSSU
SD1	40 dB	SRE	13.9531	17.5316	22.933	37.645	44.5823	37.338	**50.2155**
		RMSE	0.0069	0.0046	0.0025	0.0005	0.0002	0.0005	**0.0001**
	30 dB	SRE	8.9261	14.4408	15.7067	24.5938	34.706	27.7451	**41.9053**
		RMSE	0.0124	0.0066	0.0057	0.002	0.0006	0.0014	**0.0003**
	20 dB	SRE	4.5263	9.4239	11.3633	13.3089	20.1345	18.4413	**25.3707**
		RMSE	0.0205	0.0117	0.0093	0.0075	0.0034	0.0041	**0.0019**
SD2	40 dB	SRE	17.8794	20.6237	20.703	25.8057	27.11	25.6138	**29.6604**
		RMSE	0.007	0.0051	0.005	0.0028	0.0024	0.0029	**0.0018**
	30 dB	SRE	10.4376	18.0279	18.6229	21.7077	22.25	24.3517	**25.0497**
		RMSE	0.0164	0.0068	0.0064	0.0045	0.0042	0.0033	**0.0030**
	20 dB	SRE	4.2481	11.8626	15.0433	15.2361	14.9447	16.7237	**20.5070**
		RMSE	0.0334	0.0139	0.0096	0.0094	0.0098	0.0079	**0.0051**

larger SRE values and smaller RMSE values. It is noteworthy that the WSRSSU algorithm performs exceptionally well in unmixing low-SNR images.

In addition to quantitative evaluation, the evaluation of visual effects is also crucial. Figs. 5 and 6 show the abundance maps of the fourth endmember of SD1 and the second endmember of SD2 at 30 dB, respectively. They convey an important message: the abundance map obtained by using the SUnSAL algorithm has a large number of noise points, and the image quality is poor. The comparison between the results of SUnSAL-TV algorithm and SUnSAL proves that the spatial neighborhood information makes the abundance map smooth to a certain extent. However, the smooth transition may lose detail information. MUA$_{SLIC}$ algorithm makes use of SLIC, and it can be seen that the abundance map has obvious square areas, as shown in Fig. 5(c). Due to the influence of low-rank constraints, SUSRLR-TV and SBWCRLRU algorithms have better abundance graphs than the aforementioned methods. In other words, the difference

between the estimated abundance by WSRSSU and the reference abundance is the smallest. The spectral similarity constraint enables the abundance map to maintain more detailed information, which is the best for unmixing. Table II shows the optimal parameter setting.

B. Experiments on Real Hyperspectral Data

1) Data Details:

a) Samson data: The original data size is 925×925 pixels and each pixel has 156 bands, and its wavelength is between 401 and 889 nm [19]. The spectral resolution is up to 3.13 nm. To simplify the experiment, a local region of size 95×95 pixels was selected, which is composed of soil, tree, and water.

b) Jasper Ridge data: These data are collected by an airborne visible/infrared imaging spectrometer (AVIRIS) sensor. The original data size is 512×614 pixels and each pixel is recorded at 224 channels ranging from 380 to 2500 nm, where
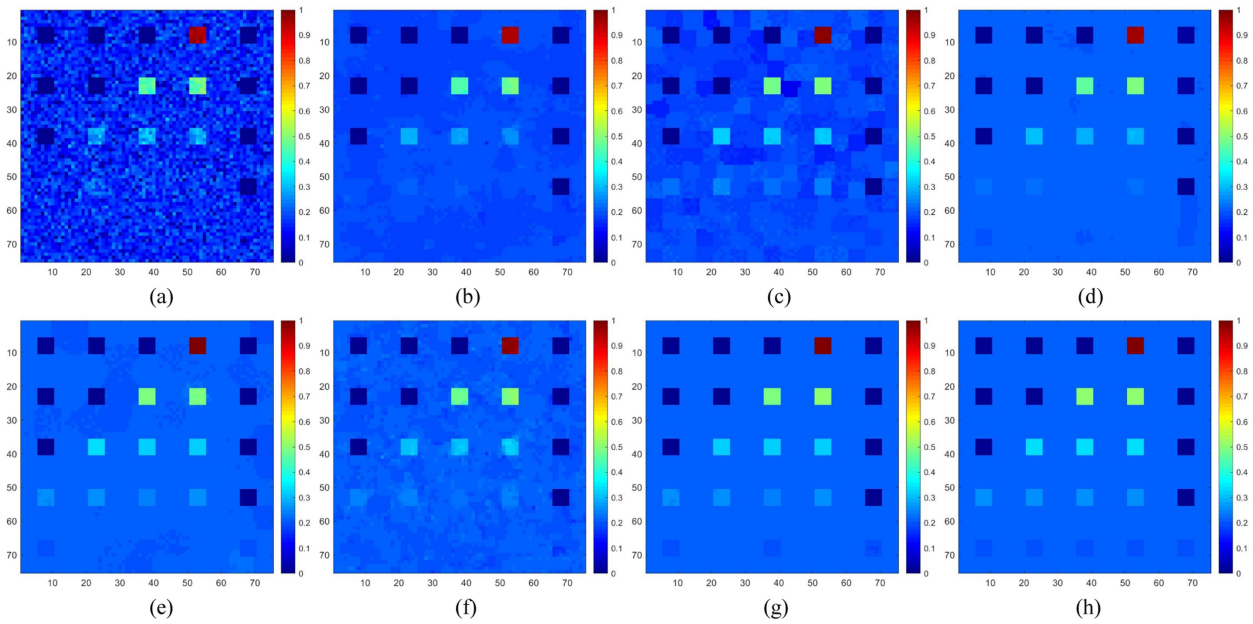
Fig. 5. Estimated abundance of SD1_30 dB. (a) SUnSAL. (b) SUnSAL-TV. (c) MUA$_{\text{SLIC}}$. (d) SUSRLR-TV. (e) SBWCRLRU. (f) RDSRSU. (g) WSRSSU. (h) Ground truth.
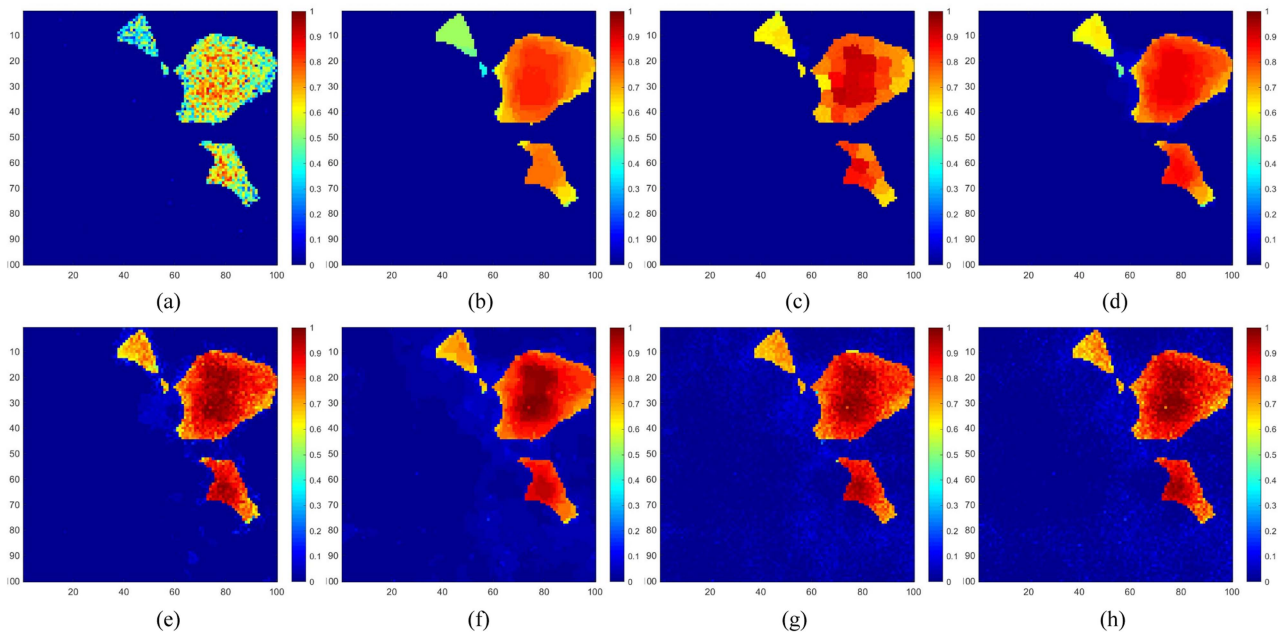

Fig. 6. Estimated abundance of SD2_30 dB. (a) SUnSAL. (b) SUnSAL-TV. (c) MUA$_{\text{SLIC}}$. (d) SUSRLR-TV. (e) SBWCRLRU. (f) RDSRSU. (g) WSRSSU. (h) Ground truth.

1–3, 108–112, 154–166, and 220–224 are noisy bands. Spectral resolution is up to 9.64 nm [24]. To simplify the experiment, the area with 100×100 pixels and 198 bands is selected as experimental data. Trees, water, dirt, and roads in this area are selected as endmembers.

c) Urban data: Compared to Samson and Jasper Ridge, Urban is a large range of data for unmixing. The data size is 307×307 pixels and each pixel has 162 bands. The spectral resolution is 10 nm. These data include six endmembers, namely asphalt, grass, tree, roof, metal, and dirt [31]. The pseudocolor images and endmember spectral curve of the three true hyperspectral data are shown in Fig. 7.

The spectral libraries of Samson, Jasper Ridge, and Urban data are constructed based on the observed images [57]. First, the pure pixels in the image are extracted to construct the initial spectral library. Afterward, to obtain the final library, the initial

TABLE II
OPTIMAL PARAMETERS OF SIMULATION DATA ON SEVEN ALGORITHMS

Algorithm	Parameter	SD1_20dB	SD1_30dB	SD1_40dB	SD2_20dB	SD2_30dB	SD2_40dB
SUnSAL	λ	7e-1	1e-1	1e-2	7e-2	1e-2	5e-3
SUnSAL-TV	λ	5e-2	7e-3	5e-3	1e-2	5e-3	5e-3
	λ_{TV}	5e-2	1e-2	1e-3	3e-2	7e-3	1e-3
MUA$_{SLIC}$	λ_1	3e-2	7e-3	1e-3	7e-3	3e-3	1e-3
	λ_2	1e-2	5e-2	1e-2	1e-1	3e-2	1e-2
	β	30	10	10	10	3	1
SUSRLR-TV	λ_{TV}	1e-2	1e-2	5e-4	3e-2	7e-3	1e-3
	ρ	5e-2	5e-2	1e-2	5e-2	1e-2	1e-2
SBWCRLRU	λ	8e-1	5e-4	5e-2	1e-2	5e-4	5e-5
	τ	5e-3	1e-1	1e-4	1e-1	3e-2	5e-3
RDSRSU	λ	1e-2	5e-3	1e-3	5e-3	5e-3	5e-3
	λ_s	4e-2	2e-2	1e-3	5e-2	5e-2	5e-2
	λ_g	3e-2	7e-3	3e-3	5e-3	5e-3	5e-3
WSRSSU	λ	5e-3	5e-3	5e-3	5e-3	5e-3	5e-3
	λ_1	1e-1	1e-2	1e-3	0.9	0.1	0.1
	λ_2	100	100	100	1	0.3	0.1
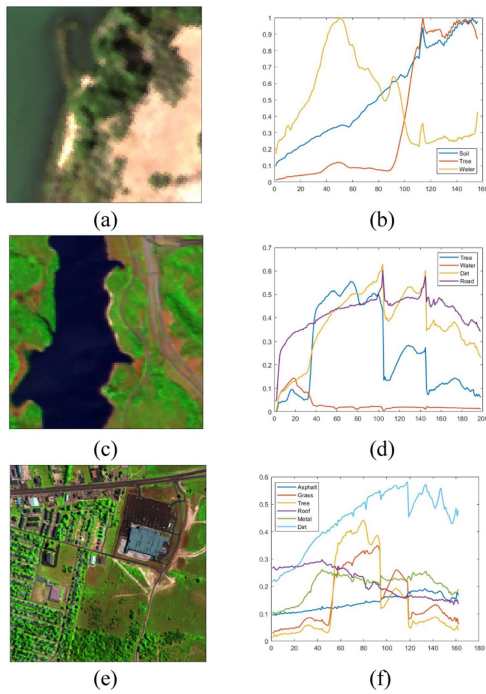
Fig. 7. Pseudocolor images and endmember spectral of Samson and Jasper. (a) Samson. (b) Endmember spectra of Samson. (c) Jasper. (d) Endmember spectra of Jasper. (e) Urban. (f) Endmember spectra of Urban.
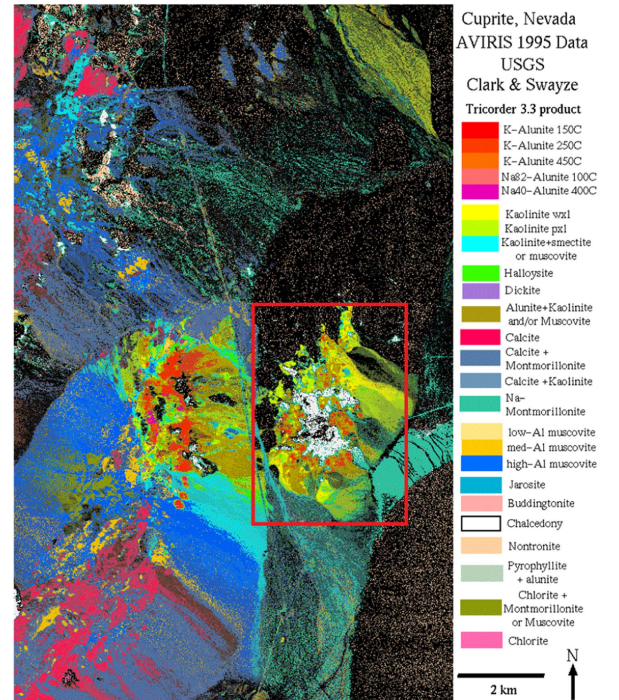

Fig. 8. Mineral distribution map of Cuprite data.

library is pruned to limit the number of signatures for each material [31].

d) Cuprite data: These data show the mineral distribution in the Cuprite area of Nevada, United States, and was collected by the AVIRIS in 1997. There are 224 channels, ranging from 370 to 2480 nm and the spatial resolution is 20 m. Only 188 bands can be used for experiment after removing the bands affected by water absorption and noise. The experimental area of containing 250×191 pixels and mineral location are shown in Fig. 8.

The spectral library for Cuprite data is the USGS library, which contains 498 mineral's spectral signatures. There are mainly 12 kinds of minerals in this area, including Alunite, Andradite, Buddingtonite, Chalcedony, Kaolinite, and other minerals [19]. The parameters of all algorithms are set according to experience. The specific description is as follows: $\lambda = 1e-3$ for SUnSAL, $\lambda = 1e-3$ and $\lambda_{TV} = 1e-3$ for SUnSAL-TV, $\lambda_2 = 1e-3$ and $\beta = 3$ for MUA$_{SLIC}$, $\lambda_{TV} = 1e-3$ and $\rho = 1e-3$ for SUSRLR-TV, $\lambda = 1e-9$ and $\tau = 1e-4$ for SRWCRLRU,

TABLE III
EVALUATION INDEXES VALUES OF SEVEN ALGORITHMS ON REAL DATA

Data	Evaluation indexes	SUnSAL	SUnSAL-TV	MUA$_{SLIC}$	SUSRLR-TV	SBWCRLRU	RDSRSU	WSRSSU
Samson	SRE	17.671	16.8739	16.1979	15.5208	17.1434	15.8073	**20.2308**
	RMSE	0.0656	0.0719	0.0777	0.084	0.0697	0.0813	**0.0489**
Jasper	SRE	16.7681	16.7246	18.0992	16.9293	17.4494	16.4496	**19.6871**
	RMSE	0.0624	0.0627	0.0535	0.0612	0.0577	0.0647	**0.0446**
Urban	SRE	9.9631	10.1437	10.648	11.4331	11.9637	12.1146	**14.4543**
	RMSE	0.1064	0.1042	0.0984	0.0899	0.0845	0.0831	**0.0635**
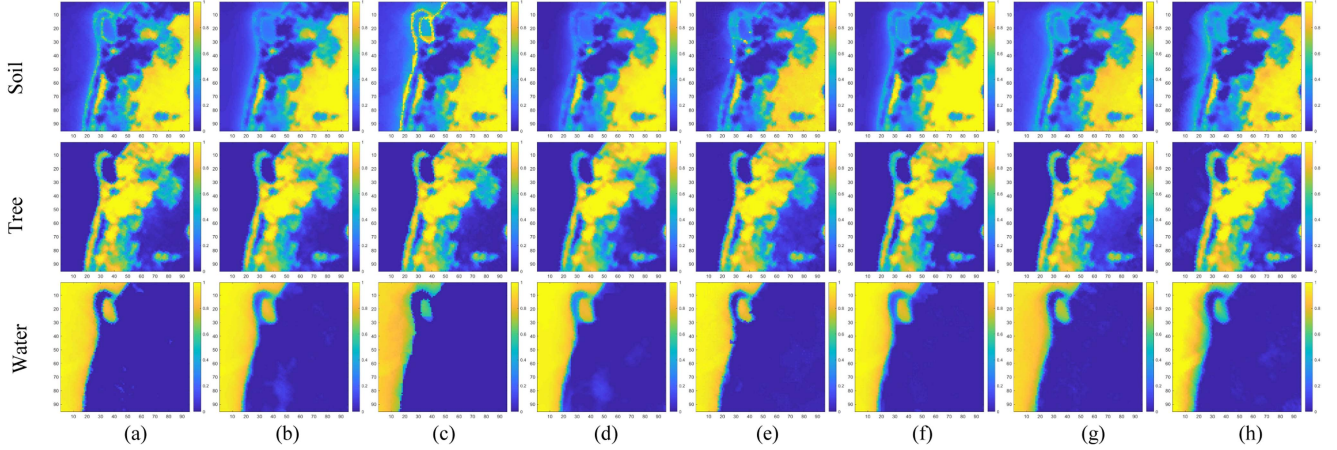
Fig. 9. Visual contrast between estimated abundance and reference abundance on Samson data. (a) SUnSAL. (b) SUnSAL-TV. (c) MUA$_{SLIC}$. (d) SUSRLR-TV. (e) SBWCRLRU. (f) RDSRSU. (g) WSRSSU. (h) Ground truth.

$\lambda_s = 5e-3$ and $\lambda_g = 1e-2$ for RDSRSU, and $\lambda_1 = 1e-2$ and $\lambda_2 = 1e-1$ for WSRSSU.

2) Result Comparison: The unmixing results of different algorithms on Samson data are displayed in Table III, and the visual comparison of the estimated abundance is shown in Fig. 9. The analysis of the Samson data unmixing results under different algorithms is as follows. First, from the perspective of SRE and RMSE, the proposed WSRSSU improves the SRE of the Samson data to 20.2308 and reduces the RMSE to 0.0489, which is better than the other six comparison algorithms. From the abundance map, it is very close to the true abundance, and there is good consistency between quantitative evaluation and visual evaluation. However, other algorithms have produced some incorrect abundances in some cases. The soil abundance of the Samson data obtained by the MUA$_{SLIC}$ algorithm is quite different from the true abundance, so some trees are wrongly identified as soil. The SUSRLR-TV algorithm cannot accurately estimate the water abundance in the Samson data.

Analyzing the abundance of data Jasper Ridge generated by different algorithms according to Table III and Fig. 10. All algorithms are good at estimating the abundance of trees, dirt, and roads, except that the estimated abundance of water is much different from the true abundance. Especially the water abundance estimated by the RDSRSU algorithm is the worst.

However, the proposed algorithm is the closest to the true abundance for the estimation of water abundance, which is better than the other six comparison algorithms.

For the Urban dataset, the abundance maps obtained through different algorithms are shown in Fig. 11. Compared with other methods, the estimated abundance of WSRSSU method is close to the true abundance. The SRE of the WSRSSU method reaches 14.4543 and the RMSE reaches 0.0635, which is significantly better than other algorithms. Table IV shows the best parameters for the three real data.

Since the Cuprite data does not have a real abundance map as reference, the performance of the algorithm cannot be measured quantitatively. Fig. 12 shows the estimated abundance maps of 12 endmembers in the Cuprite data. Alunite, Buddingtonite, and Chalcedony are often selected as representatives of the region to analyze the performance of algorithms. It can be concluded that the SUnSAL method has the worst effect in estimating abundance. The abundance maps obtained by the RDSRSU method are overly smooth, especially Buddingtonite and Chalcedony. Compared with other methods, the WSRSSU method has better unmixing results. From the evaluation indexes and estimated abundance maps of four real data, it can be seen that the proposed algorithm can obtain significant results. In summary, the WSRSSU algorithm is an effective unmixing method.
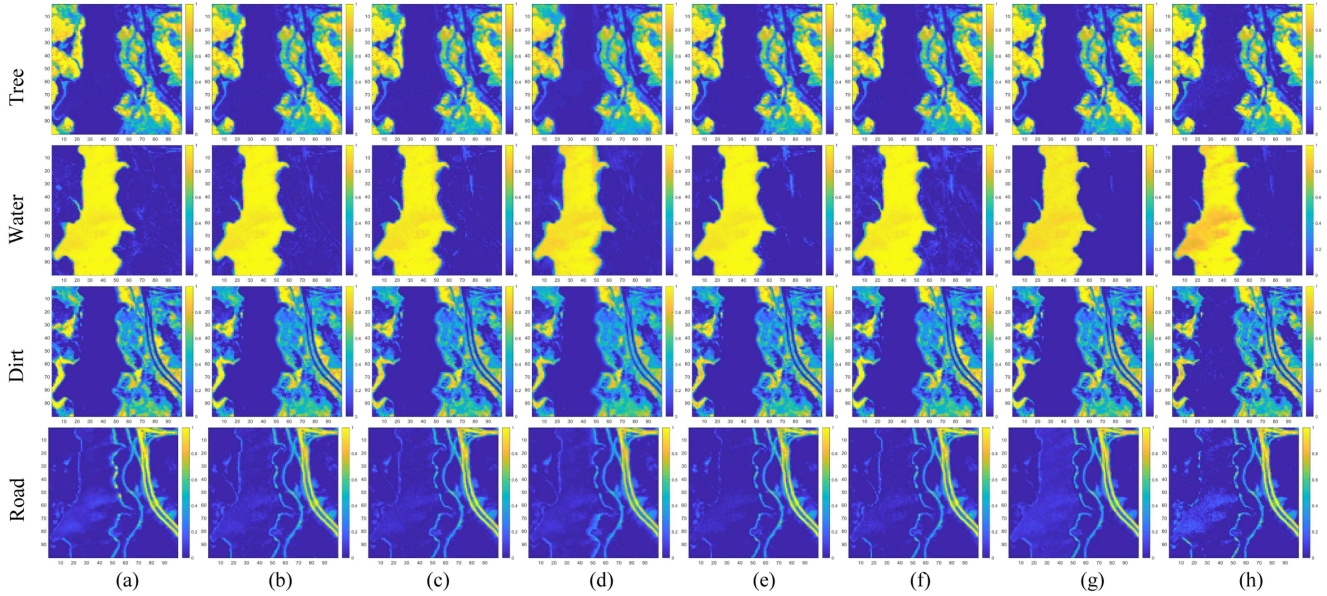
Fig. 10. Visual contrast between estimated abundance and reference abundance on Jasper data. (a) SUnSAL. (b) SUnSAL-TV. (c) MUA$_{SLIC}$. (d) SUSRLR-TV. (e) SBWCRLRU. (f) RDSRSU. (g) WSRSSU. (h) Ground truth.

TABLE IV
OPTIMAL PARAMETERS OF REAL DATA ON SEVEN ALGORITHMS

Algorithm	Parameter	Samson	Jasper	Urban
SUnSAL	λ	1e-2	1e-2	1e-2
SUnSAL-TV	λ	5e-3	5e-3	5e-3
	λ_{TV}	7e-3	7e-3	7e-3
MUA$_{SLIC}$	λ_1	7e-3	1e-3	5e-3
	λ_2	7e-2	1e-2	1e-2
	β	3	3	3
SUSRLR-TV	λ_{TV}	5e-2	1e-2	1e-3
	ρ	1e-2	1e-1	1e-2
SBWCRLRU	λ	1e-2	1e-4	1e-3
	τ	1e-2	1e-3	0
RDSRSU	λ	5e-3	5e-3	5e-3
	λ_s	1.5	1e-3	1e-2
	λ_g	1e-2	1e-3	1e-3
WSRSSU	λ	1e-2	5e-3	5e-3
	λ_1	1.2	1e-2	2e-1
	λ_2	1e-2	2e-1	5e-2

V. DISCUSSIONS

To illustrate the effect of WSRSSU algorithm is valid, the experiments of synthetic data on four different parameters are concerned. The four parameters are the regularization parameter λ_1, λ_2, the penalty parameter μ, number of superpixels, and K. For convenience, the experimental results of SD1 and SD2 at 30 dB with the changes of four parameters are analyzed. And we conducted a convergence analysis of the algorithm, which are as follows.

1) *Regularization parameter analysis:* In the proposed WSRSSU algorithm, the objective function includes the regularization parameters λ_1 and λ_2. Parameter λ_1

represents the influence of weighted sparsity on unmixing, and parameter λ_2 represents the influence of spectral similarity constraint on unmixing. For SD1, the penalty parameter μ is set to 0.1 temporarily, and then λ_1 and λ_2 are selected from the set $\{0, 0.001, 0.01, 0.1, 0.2, 0.3, 0.4, 0.5, 0.6, 0.7, 0.8, 0.9, 1\}$ and the set $\{0, 0.001, 0.01, 0.1, 0.2, 0.3, 0.4, 0.5, 0.6, 0.7, 0.8, 0.9, 1, 10, 100, 1000, 10\,000\}$, respectively. Based on the unmixing results of different λ_1 and λ_2 combinations, the optimize parameters are used for subsequent experiments. As shown in Fig. 13(a), SRE reaches a peak at a certain position and then decreases. Therefore, $\lambda_1 = 0.01$ and $\lambda_2 = 100$ to SD1. Temporarily μ of SD2 is set to 0.1, and then λ_1 and λ_2 are selected from
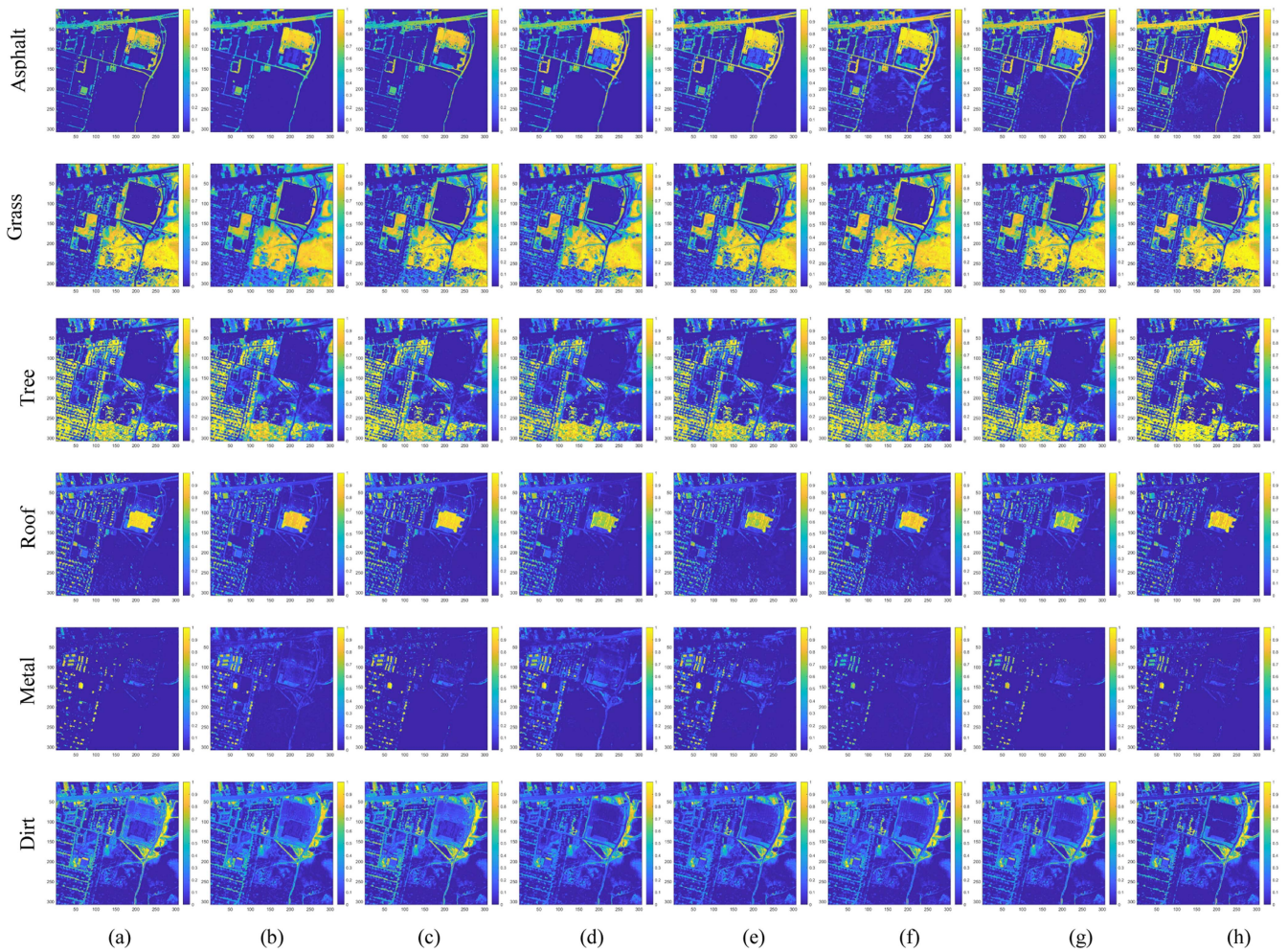
Fig. 11. Visual contrast between estimated abundance and reference abundance on Urban data. (a) SUnSAL. (b) SUnSAL-TV. (c) MUA$_{SLIC}$. (d) SUSRLR-TV. (e) SBWCRLRU. (f) RDSRSU. (g) WSRSSU. (h) Ground truth.

the set {0, 0.001, 0.01, 0.1, 0.2, 0.3, 0.4, 0.5, 0.6, 0.7, 0.8, 0.9, 1}. From Fig. 13(c) and (d), it can be seen that λ_1 and λ_2 tend to be stable at 0.1–1. Finally, $\lambda_1 = 0.1$, and $\lambda_2 = 0.3$ to SD2.

2) *Penalty parameter analysis:* When analyzing the penalty parameter μ, the regularization parameter λ_1 and λ_2 are fixed at their optimal values obtained in 1). The range of values for parameter μ is {0, 0.001, 0.01, 0.1, 0.2, 0.3, 0.4, 0.5, 0.6, 0.7, 0.8, 0.9, 1}. Following the same process as before, the optimal μ for SD1 and SD2 is determined based on the SRE and RMSE metrics. The unmixing results obtained for different μ values are shown in Fig. 14. For SD1, μ is set to 0.6. For SD2, μ is set to 0.5.

3) *Number of superpixels and K analysis:* In this section, the experiments of SD1 and SD2 at 30 dB are used as examples to discuss the influence of different numbers of superpixels and K on unmixing. For SD1, the number of superpixels was set to {1, 4, 9, 16, 25, 36, 49, 64, 81, 100, 121, 169, 225, 361, 625}. For SD2, the number of superpixels was set to {1, 4, 15, 25, 49, 64, 81, 100, 144,

169, 225, 289, 400, 625}. The value range of K is set to {5, 6, 7, 8, 9, 10, 11, 12, 13, 14, 15} for SD1 and SD2.

Fig. 15 shows the changes of SRE and RMSE with the number of superpixels and K. From the results, it is found that when the number of superpixels is 1 and K is 14, the SD1 has the best unmixing result, with the largest SRE and the smallest RMSE. SD2 has the best abundance estimation when the number of superpixels is 25 and K is 12.

4) *Effectiveness of weighted sparse constraint:* To analyze the effectiveness of weighted sparse constraint, two experiments were designed: an experiment without weighted sparse constraint and an experiment with weighted sparse constraint. The SRE and RMSE of two experiments were compared. Fig. 16 shows weighted sparse unmixing method estimates more accurate abundance, which means that weighted sparse constraint plays a positive role in unmixing.

5) *Effectiveness of spectral similarity constraint:* To demonstrate the effectiveness of spectral similarity constraint in unmixing, the precisions of experiments without spectral
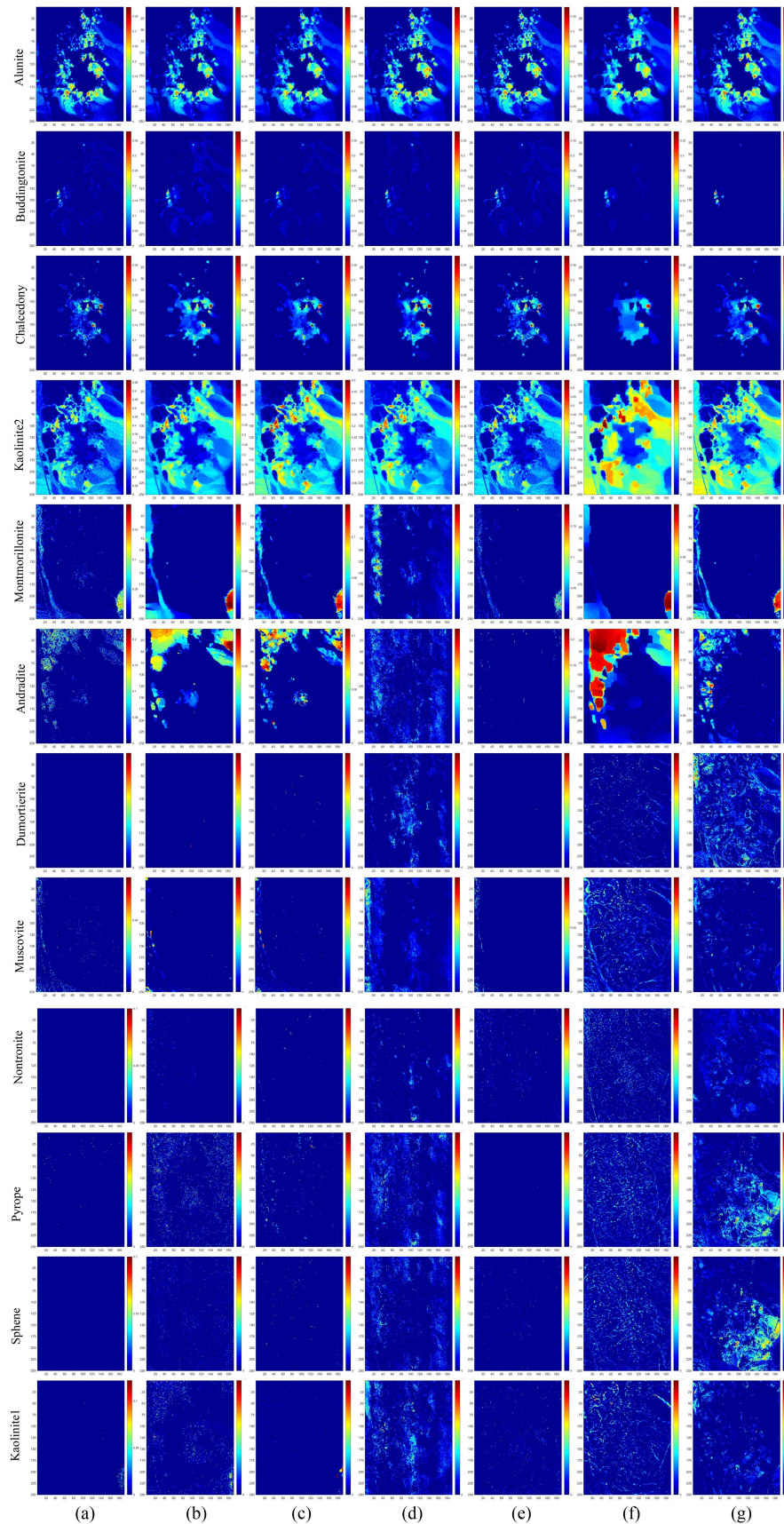
Fig. 12. Estimated abundance of Cuprite data. (a) SUnSAL. (b) SUnSAL-TV. (c) MUA$_{SLIC}$. (d) SUSRLR-TV. (e) SBWCRLRU. (f) RDSRSU. (g) WSRSSU.
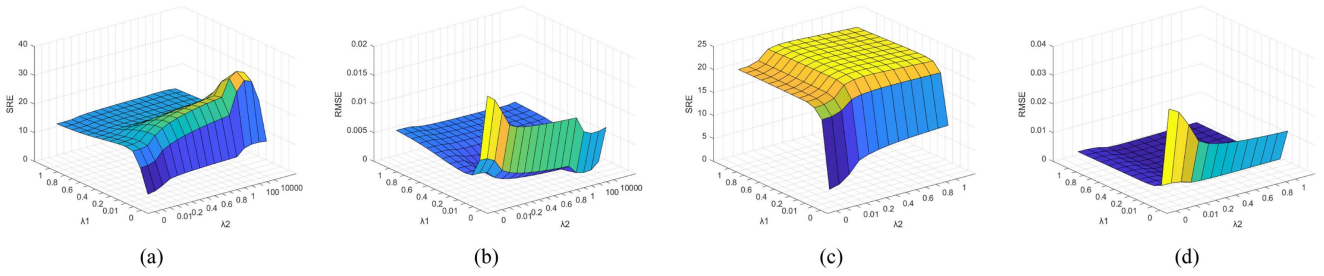
Fig. 13. Response of evaluation indexes to parameters λ_1 and λ_2 for WSRSSU algorithm. (a) and (b) SD1. (c) and (d) SD2.
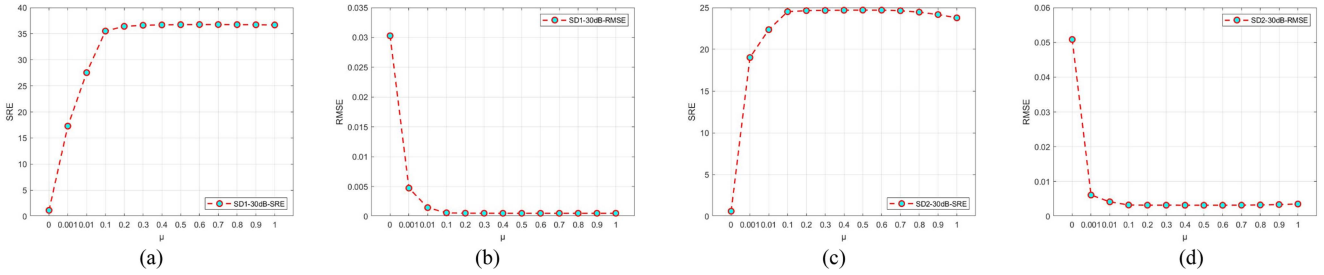

Fig. 14. Response of evaluation indexes to parameter μ for WSRSSU algorithm. (a) and (b) SD1. (c) and (d) SD2.
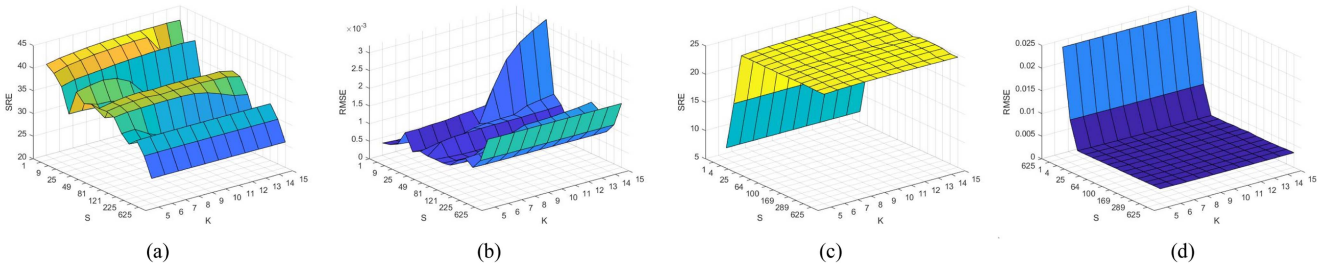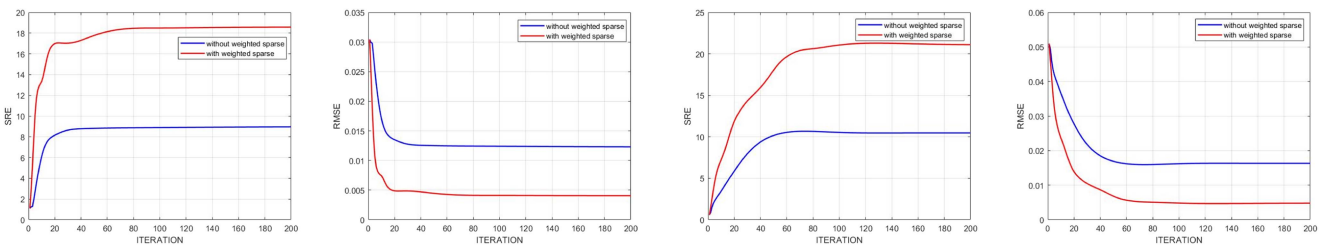

Fig. 15. Response of evaluation indexes to parameters K and number of superpixels for WSRSSU algorithm. (a) and (b) SD1. (c) and (d) SD2.

Fig. 16. Response of evaluation indexes to weighted sparse constraint. (a), (b), (c), and (d).

similarity constraint and experiments with spectral similarity constraint were compared. From Fig. 17, it can be concluded that spectral similarity constraints are effective.

6) *Effectiveness of optimal neighbors:* Choosing the optimal neighbors is crucial for unmixing. To analyze the effectiveness of optimal neighbors, experiments were designed on the synthetic data for selecting K neighbors or selecting all neighbors. From Fig. 18, it can be concluded that selecting

the best neighbors for unmixing is better than not selecting the best neighbors. Therefore, it is proven that the optimal neighborhood pixels are effective for unmixing.

7) *Convergence analysis:* In order to analyze the convergence of the algorithm, SRE and RMSE are used as functions of the number of iterations to obtain the convergence curve. Fig. 19 shows that when the number of iterations approaches 200, the values of SRE and RMSE remain almost
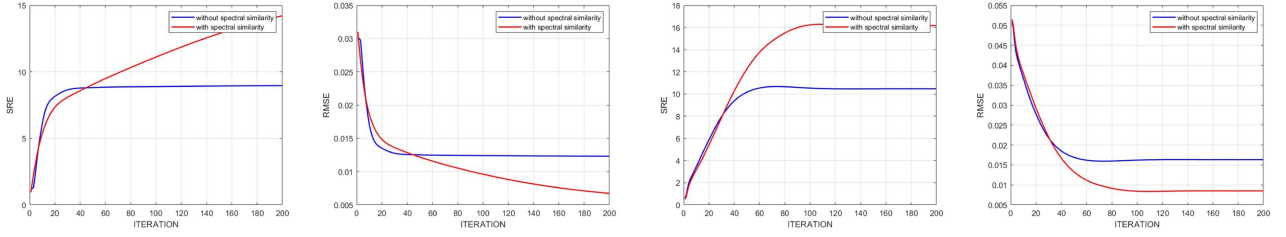
Fig. 17.   Response of evaluation indexes to spectral similarity constraint. (a), (b), (c), and (d).
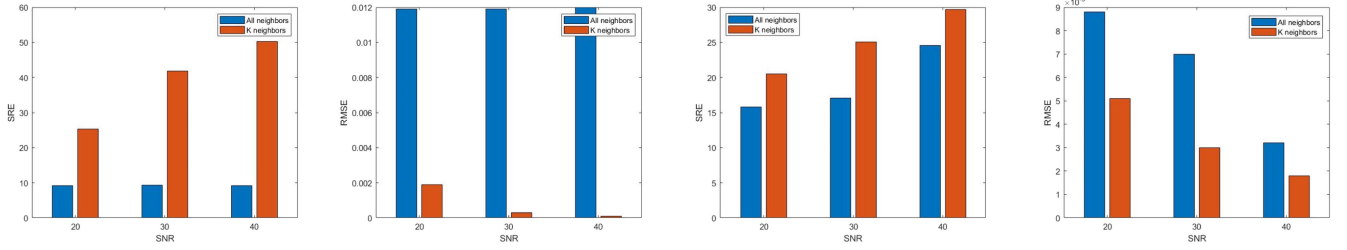

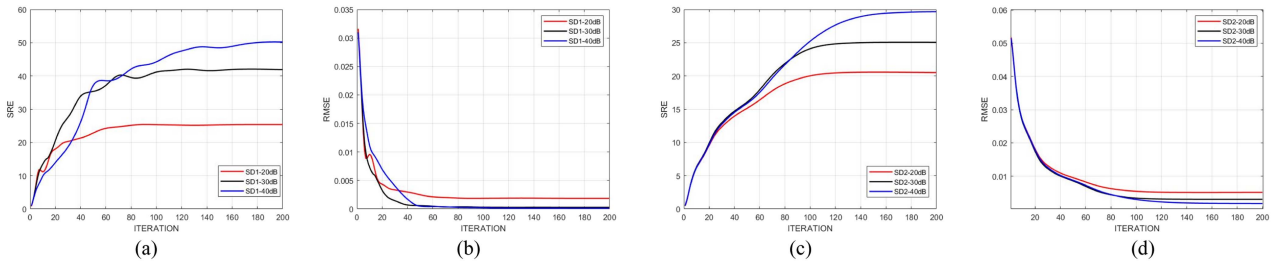Fig. 18.   Response of evaluation indexes to different neighbors. (a), (b), (c), and (d).

Fig. 19.   Response of evaluation indexes to iterations for WSRSSU algorithm. (a) and (b) SD1. (c) and (d) SD2.

TABLE V
RUNTIME OF ALL ALGORITHMS ON DIFFERENT DATA

	Data	SUnSAL	SUnSAL-TV	MUA$_{SLIC}$	SUSRLR-TV	SBWCRLRU	RDSRSU	WSRSSU
	SD1	7.612	114.625	13.811	150.608	132.261	118.429	2688.9269
	SD2	13.741	147.991	10.699	214.294	207.541	160.667	199
Runtime	**Samson**	10.3194	86.5927	8.7198	115.8295	76.0827	97.0363	206.1528
(second)	**Jasper**	57.4477	325.611	87.4701	588.1076	551.1584	437.7699	570.6062
	Urban	91.7271	1326.979	667.0721	1921.2868	1749.9046	850.0002	269.8940
	Cuprite	301.024	1806.864	183.184	2623.982	1810.502	1999.334	518.03

unchanged, which is sufficient to prove the convergence of WSRSSU. The running time of all algorithms on all data is shown in Table V. The SUnSAL method takes less time, whereas the WSRSSU method takes more time due to the selection of neighboring pixels.

VI. CONCLUSION

This article proposes a new algorithm for HU, which is based on the framework of sparse unmixing. The WSRSSU algorithm uses image segmentation to construct local regions, and then makes full use of the spatial–spectral information of

the image from the perspective of sparsity enhancement and spectral similarity constraint. The experimental results show that it can offer more accurate abundance estimation results and abundance graphs, and also demonstrate that the weighted sparse regularization and the spectral similarity regularization of a local region have a positive effect for unmixing.

unmixing by superpixel-based reweighted low-rank and total variation (SUSRLR-TV) code, and Prof. J. Bioucas-Dias for sharing sparse unmixing by variable splitting and augmented Lagrangian-total variation (SUnSAL-TV) code. The authors would also like to thank editors, associated editors, and anonymous reviewers for their insightful suggestions and comments, which significantly improve this article.

REFERENCES

[1] J. Feng et al., "Deep reinforcement learning for semisupervised hyperspectral band selection," *IEEE Trans. Geosci. Remote Sens.*, vol. 60, Feb. 2022, Art. no. 5501719.

[2] H. Su, Z. Wu, A. X. Zhu, and Q. Du, "Low rank and collaborative representation for hyperspectral anomaly detection via robust dictionary construction," *ISPRS J. Photogrammetry Remote Sens.*, vol. 169, pp. 195–211, 2020.

[3] H. Su, Y. Yu, Q. Du, and P. Du, "Ensemble learning for hyperspectral image classification using tangent collaborative representation," *IEEE Trans. Geosci. Remote Sens.*, vol. 58, no. 6, pp. 3778–3790, Jun. 2020.

[4] P. Zheng, H. Su, H. Lu, and Q. Du, "Adaptive hypergraph regularized multilayer sparse tensor factorization for hyperspectral unmixing," *IEEE Trans. Geosci. Remote Sens.*, vol. 61, Jan. 2023, Art. no. 5502918.

[5] H. Su, W. Yao, Z. Wu, P. Zheng, and Q. Du, "Kernel low-rank representation with elastic net for China coastal wetland land cover classification using GF-5 hyperspectral imagery," *ISPRS J. Photogrammetry Remote Sens.*, vol. 171, pp. 238–252, 2021.

[6] D. Mao et al., "Remote observations in China's Ramsar sites: Wetland dynamics, anthropogenic threats, and implications for sustainable development goals," *J. Remote Sens.*, vol. 2021, 2021, Art. no. 9849343.

[7] A. Zare and K. C. Ho, "Endmember variability in hyperspectral analysis: Addressing spectral variability during spectral unmixing," *IEEE Signal Process. Mag.*, vol. 31, no. 1, pp. 95–104, Jan. 2014.

[8] H. Su, Z. Wu, H. Zhang, and Q. Du, "Hyperspectral anomaly detection: A survey," *IEEE Geosci. Remote Sens. Mag.*, vol. 10, no. 1, pp. 64–90, Mar. 2022.

[9] G. Cheng, C. Lang, M. Wu, X. Xie, X. Yao, and J. Han, "Feature enhancement network for object detection in optical remote sensing images," *J. Remote Sens.*, vol. 2021, pp. 1–14, 2021.

[10] P. Ghamisi et al., "Advances in hyperspectral image and signal processing: A comprehensive overview of the state of the art," *IEEE Geosci. Remote Sens. Mag.*, vol. 5, no. 4, pp. 37–78, Dec. 2017.

[11] J. M. Bioucas-Dias et al., "Hyperspectral unmixing overview: Geometrical, statistical, and sparse regression-based approaches," *IEEE J. Sel. Topics Appl. Earth Observ. Remote Sens.*, vol. 5, no. 2, pp. 354–379, Apr. 2012.

[12] N. Dobigeon, J.-Y. Tourneret, C. Richard, J. C. M. Bermudez, S. McLaughlin, and A. O. Hero, "Nonlinear unmixing of hyperspectral images: Models and algorithms," *IEEE Signal Process. Mag.*, vol. 31, no. 1, pp. 82–94, Jan. 2014.

[13] M.-D. Iordache, J. M. Bioucas-Dias, and A. Plaza, "Sparse unmixing of hyperspectral data," *IEEE Trans. Geosci. Remote Sens.*, vol. 49, no. 6, pp. 2014–2039, Jun. 2011.

[14] F. Li, S. Zhang, C. Deng, B. Liang, J. Cao, and S. Wang, "Robust double spatial regularization sparse hyperspectral unmixing," *IEEE J. Sel. Topics Appl. Earth Observ. Remote Sens.*, vol. 14, pp. 12569–12582, Dec. 2021.

[15] J. M. P. Nascimento and J. M. B. Dias, "Vertex component analysis: A fast algorithm to unmix hyperspectral data," *IEEE Trans. Geosci. Remote Sens.*, vol. 43, no. 4, pp. 898–910, Apr. 2005.

[16] J. M. Bioucas-Dias, "A variable splitting augmented Lagrangian approach to linear spectral unmixing," in *Proc. 1st Workshop Hyperspectral Image Signal Process.: Evol. Remote Sens.*, 2009, pp. 1–4.

[17] J. Li and J. M. Bioucas-Dias, "Minimum volume simplex analysis: A fast algorithm to unmix hyperspectral data," in *Proc. IEEE Int. Geosci. Remote Sens. Symp.*, 2008, pp. III–250–III–253.

[18] N. Wang, B. Du, L. Zhang, and L. Zhang, "An abundance characteristic-based independent component analysis for hyperspectral unmixing," *IEEE Trans. Geosci. Remote Sens.*, vol. 53, no. 1, pp. 416–428, Jan. 2015.

[19] X.-R. Feng, H.-C. Li, R. Wang, Q. Du, X. Jia, and A. Plaza, "Hyperspectral unmixing based on nonnegative matrix factorization: A comprehensive review," *IEEE J. Sel. Topics Appl. Earth Observ. Remote Sens.*, vol. 15, pp. 4414–4436, May 2022.

[20] L. Dong, Y. Yuan, and X. Lu, "Spectral–spatial joint sparse NMF for hyperspectral unmixing," *IEEE Trans. Geosci. Remote Sens.*, vol. 59, no. 3, pp. 2391–2402, Mar. 2021.

[21] R. Huang, X. Li, and L. Zhao, "Spectral–spatial robust nonnegative matrix factorization for hyperspectral unmixing," *IEEE Trans. Geosci. Remote Sens.*, vol. 57, no. 10, pp. 8235–8254, Oct. 2019.

[22] L. Tong, J. Zhou, B. Qian, J. Yu, and C. Xiao, "Adaptive graph regularized multilayer nonnegative matrix factorization for hyperspectral unmixing," *IEEE J. Sel. Topics Appl. Earth Observ. Remote Sens.*, vol. 13, pp. 434–447, Jan. 2020.

[23] X. Wang, Y. Zhong, L. Zhang, and Y. Xu, "Spatial group sparsity regularized nonnegative matrix factorization for hyperspectral unmixing," *IEEE Trans. Geosci. Remote Sens.*, vol. 55, no. 11, pp. 6287–6304, Nov. 2017.

[24] J. Peng, Y. Zhou, W. Sun, Q. Du, and L. Xia, "Self-paced nonnegative matrix factorization for hyperspectral unmixing," *IEEE Trans. Geosci. Remote Sens.*, vol. 59, no. 2, pp. 1501–1515, Feb. 2021.

[25] L. Miao and H. Qi, "Endmember extraction from highly mixed data using minimum volume constrained nonnegative matrix factorization," *IEEE Trans. Geosci. Remote Sens.*, vol. 45, no. 3, pp. 765–777, Mar. 2007.

[26] G. Zhang, S. Mei, Y. Feng, and Q. Du, "Spectral-spatial constrained nonnegative matrix factorization for spectral mixture analysis of hyperspectral images," *IEEE J. Sel. Topics Appl. Earth Observ. Remote Sens.*, vol. 14, pp. 6766–6776, Jun. 2021.

[27] J. M. Bioucas-Dias and M. A. T. Figueiredo, "Alternating direction algorithms for constrained sparse regression application to hyperspectral unmixing," in *Proc. 2nd Workshop Hyperspectral Image Signal Process.: Evol. Remote Sens.*, 2010, pp. 1–4.

[28] M.-D. Iordache, J. M. Bioucas-Dias, and A. Plaza, "Total variation spatial regularization for sparse hyperspectral unmixing," *IEEE Trans. Geosci. Remote Sens.*, vol. 50, no. 11, pp. 4484–4502, Nov. 2012.

[29] S. Zhang, J. Li, H.-C. Li, C. Deng, and A. Plaza, "Spectral–spatial weighted sparse regression for hyperspectral image unmixing," *IEEE Trans. Geosci. Remote Sens.*, vol. 56, no. 6, pp. 3265–3276, Jun. 2018.

[30] R. Wang, H.-C. Li, W. Liao, and A. Pižurica, "Double reweighted sparse regression for hyperspectral unmixing," in *Proc. IEEE Int. Geosci. Remote Sens. Symp.*, 2016, pp. 6986–6989.

[31] R. A. Borsoi, T. Imbiriba, J. C. M. Bermudez, and C. Richard, "A fast multiscale spatial regularization for sparse hyperspectral unmixing," *IEEE Geosci. Remote Sens. Lett.*, vol. 16, no. 4, pp. 598–602, Apr. 2019.

[32] H. Li, R. Feng, L. Wang, Y. Zhong, and L. Zhang, "Superpixel-based reweighted low-rank and total variation sparse unmixing for hyperspectral remote sensing imagery," *IEEE Trans. Geosci. Remote Sens.*, vol. 59, no. 1, pp. 629–647, Jan. 2021.

[33] H. Su, C. Jia, P. Zheng, and Q. Du, "Superpixel-based weighted collaborative sparse regression and reweighted low-rank representation for hyperspectral image unmixing," *IEEE J. Sel. Topics Appl. Earth Observ. Remote Sens.*, vol. 15, pp. 393–408, Dec. 2022.

[34] W. Tang, Z. Shi, Y. Wu, and C. Zhang, "Sparse unmixing of hyperspectral data using spectral a priori information," *IEEE Trans. Geosci. Remote Sens.*, vol. 53, no. 2, pp. 770–783, Feb. 2015.

[35] M.-D. Iordache, J. M. Bioucas-Dias, and A. Plaza, "Collaborative sparse regression for hyperspectral unmixing," *IEEE Trans. Geosci. Remote Sens.*, vol. 52, no. 1, pp. 341–354, Jan. 2014.

[36] E. J. Candès, M. B. Wakin, and S. P. Boyd, "Enhancing sparsity by reweighted ℓ_1 minimization," *J. Fourier Anal. Appl.*, vol. 14, no. 5/6, pp. 877–905, 2008.

[37] X. Zhang, P. Weng, J. Feng, E. Zhang, and B. Hou, "Spatial-spectral classification based on group sparse coding for hyperspectral image," in *Proc. IEEE Int. Geosci. Remote Sens. Symp.*, 2013, pp. 1745–1748.

[38] S. Mei, G. Zhang, J. Li, Y. Zhang, and Q. Du, "Improving spectral-based endmember finding by exploring spatial context for hyperspectral unmixing," *IEEE J. Sel. Topics Appl. Earth Observ. Remote Sens.*, vol. 13, pp. 3336–3349, Jun. 2020.

[39] S. Mei, M. He, Z. Wang, and D. Feng, "Spatial purity based endmember extraction for spectral mixture analysis," *IEEE Trans. Geosci. Remote Sens.*, vol. 48, no. 9, pp. 3434–3445, Sep. 2010.

[40] R. Wang, H.-C. Li, A. Pizurica, J. Li, A. Plaza, and W. J. Emery, "Hyperspectral unmixing using double reweighted sparse regression and total variation," *IEEE Geosci. Remote Sens. Lett.*, vol. 14, no. 7, pp. 1146–1150, Jul. 2017.

[41] R. Ammanouil, A. Ferrari, and C. Richard, "A graph Laplacian regularization for hyperspectral data unmixing," in *Proc. IEEE Int. Conf. Acoust., Speech Signal Process.*, 2015, pp. 1637–1641.

[42] P. V. Giampouras, K. E. Themelis, A. A. Rontogiannis, and K. D. Koutroumbas, "Simultaneously sparse and low-rank abundance matrix estimation for hyperspectral image unmixing," *IEEE Trans. Geosci. Remote Sens.*, vol. 54, no. 8, pp. 4775–4789, Aug. 2016.

[43] J. Huang, T.-Z. Huang, L.-J. Deng, and X.-L. Zhao, "Joint-sparse-blocks and low-rank representation for hyperspectral unmixing," *IEEE Trans. Geosci. Remote Sens.*, vol. 57, no. 4, pp. 2419–2438, Apr. 2019.

[44] X. Zhang et al., "Hyperspectral unmixing via low-rank representation with space consistency constraint and spectral library pruning," *Remote Sens.*, vol. 10, no. 2, 2018, Art. no. 339.

[45] J. Li, Y. Li, R. Song, S. Mei, and Q. Du, "Local spectral similarity preserving regularized robust sparse hyperspectral unmixing," *IEEE Trans. Geosci. Remote Sens.*, vol. 57, no. 10, pp. 7756–7769, Oct. 2019.

[46] S. Zhang et al., "Double regression-based sparse unmixing for hyperspectral images," *J. Sensors*, vol. 2021, pp. 1–14, 2021.

[47] T. Ince, "Double spatial graph Laplacian regularization for sparse unmixing," *IEEE Geosci. Remote Sens. Lett.*, vol. 19, Mar. 2022, Art. no. 8009605.

[48] S. Zhang, W. Hua, G. Li, J. Liu, and Q. Wang, "Superpixel and low-rank double-sparse regression hyperspectral unmixing," *J. Appl. Remote Sens.*, vol. 15, no. 3, 2021, Art. no. 032205.

[49] R. Achanta, A. Shaji, K. Smith, A. Lucchi, P. Fua, and S. Susstrunk, "SLIC superpixels compared to state-of-the-art superpixel methods," *IEEE Trans. Pattern Anal. Mach. Intell.*, vol. 34, no. 11, pp. 2274–2282, Nov. 2012.

[50] B. K. Natarajan, "Sparse approximate solutions to linear systems," *SIAM J. Comput.*, vol. 24, no. 2, pp. 227–234, 1995.

[51] S. Subudhi, R. N. Patro, P. K. Biswal, and F. Dell'Acqua, "A survey on superpixel segmentation as a preprocessing step in hyperspectral image analysis," *IEEE J. Sel. Topics Appl. Earth Observ. Remote Sens.*, vol. 14, pp. 5015–5035, Apr. 2021.

[52] F. Xiong, J. Chen, J. Zhou, and Y. Qian, "Superpixel-based nonnegative tensor factorization for hyperspectral unmixing," in *Proc. IEEE Int. Geosci. Remote Sens. Symp.*, 2018, pp. 6392–6395.

[53] W. Sun, J. Ma, G. Yang, B. Du, and L. Zhang, "A Poisson nonnegative matrix factorization method with parameter subspace clustering constraint for endmember extraction in hyperspectral imagery," *ISPRS J. Photogrammetry Remote Sens.*, vol. 128, pp. 27–39, 2017.

[54] Y. Jin, Y. Dong, Y. Zhang, and X. Hu, "SSMD: Dimensionality reduction and classification of hyperspectral images based on spatial–spectral manifold distance metric learning," *IEEE Trans. Geosci. Remote Sens.*, vol. 60, Sep. 2022, Art. no. 5538916.

[55] X.-H. Han, B. Shi, and Y. Zheng, "Self-similarity constrained sparse representation for hyperspectral image super-resolution," *IEEE Trans. Image Process.*, vol. 27, no. 11, pp. 5625–5637, Nov. 2018.

[56] W. Zuo, D. Meng, L. Zhang, X. Feng, and D. Zhang, "A generalized iterated shrinkage algorithm for non-convex sparse coding," in *Proc. IEEE Int. Conf. Comput. Vis.*, 2013, pp. 217–224.

[57] B. Somers, M. Zortea, A. Plaza, and G. P. Asner, "Automated extraction of image-based endmember bundles for improved spectral unmixing," *IEEE J. Sel. Topics Appl. Earth Observ. Remote Sens.*, vol. 5, no. 2, pp. 396–408, Apr. 2012.

Guoguo Yang received the M.S. degree in ecology from Henan Agricultural University, Zhengzhou, China, in 2001, and the Ph.D. degree in ecology from the College of Resources and Environmental Sciences, Nanjing Agricultural University, Nanjing, China, in 2022.

Since 2023, she has been a Research Assistant with the School of Geographic Information and Tourism, Chuzhou University, Chuzhou, China. Her research interests include hyperspectral remote sensing and quantitative inversion of remote sensing of soil parameters.

Qian Du (Fellow, IEEE) received the Ph.D. degree in electrical engineering from the University of Maryland, Baltimore, MD, USA, in 2000.

She is currently the Bobby Shackouls Professor with the Department of Electrical and Computer Engineering, Mississippi State University, Starkville, MS, USA. Her research interests include hyperspectral image analysis and applications, pattern classification, data compression, and neural networks.

Dr. Du is a Fellow of the SPIE-International Society for Optics and Photonics. She was a Co-Chair of the Data Fusion Technical Committee of the IEEE Geoscience and Remote Sensing Society from 2009 to 2013, and the Chair of the Remote Sensing and Mapping Technical Committee of the International Association for Pattern Recognition from 2010 to 2014. She was an Associate Editor for the IEEE JOURNAL OF SELECTED TOPICS IN APPLIED EARTH OBSERVATIONS AND REMOTE SENSING, *Journal of Applied Remote Sensing*, *IEEE Signal Processing Letters*, IEEE TRANSACTIONS ON GEOSCIENCE AND REMOTE SENSING, PATTERN RECOGNITION, and MDPI *Remote Sensing*. During 2016–2020, she was the Editor-in-Chief for the IEEE JOURNAL OF SELECTED TOPICS IN APPLIED EARTH OBSERVATIONS AND REMOTE SENSING. She is currently a Member of the IEEE Periodicals Review and Advisory Committee and SPIE Publications Committee.

Yao Liang received the B.E. degree in remote sensing science and technology from the School of Mining and Geomatics Engineering, Hebei University of Engineering, Handan, China, in 2021. She is currently working toward the M.E. degree in surveying and mapping with the School of Earth Sciences and Engineering, Hohai University, Nanjing, China.

Her research interests include sparse representation and machine learning in hyperspectral unmixing.

Hengyi Zheng is currently working toward the B.E. degree in geomatics engineering from the School of Earth Sciences and Engineering, Hohai University, Nanjing, China.

Her research interests include collaborative representation and hyperspectral remote sensing imagery classification.

Hongjun Su (Senior Member, IEEE) received the Ph.D. degree in cartography and geography information system from the Key Laboratory of Virtual Geographic Environment (Ministry of Education), Nanjing Normal University, Nanjing, China, in 2011.

He is currently a Full Professor with the School of Earth Sciences and Engineering, Hohai University, Nanjing, China. His main research interests include hyperspectral remote sensing dimensionality reduction, classification, and spectral unmixing.

Dr. Su is an Associate Editor for the IEEE JOURNAL OF SELECTED TOPICS IN APPLIED EARTH OBSERVATIONS AND REMOTE SENSING. He was the recipient of the 2016 Best Reviewer Award from the IEEE Geoscience and Remote Sensing Society.